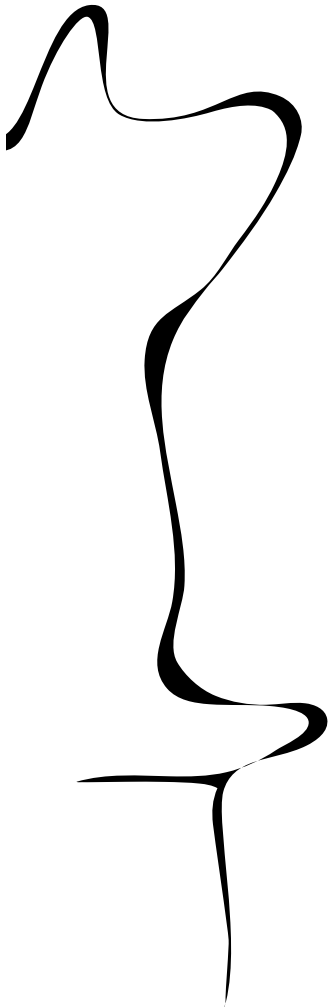


Faculty of Engineering Technology (CTW)

Model Predictive Control of Forming Processes
Master Thesis



s1116754 **B. M. DE GOOIJER**



Examination Committee:
prof. dr. ir. A. H. VAN DEN BOOGAARD
prof. dr. ir. R. AKKERMAN
dr. ir. H. J. M. GEIJSELAERS
ir. G. T. HAVINGA

Date:
August 31, 2015

Document Number:
CTW.15/TM-5759

UNIVERSITY OF TWENTE.

Model Predictive Control of Forming Processes
Master Thesis

s1116754 **BOUKJE MARIJE DE GOOIJER**

Institution:

University of Twente
Faculty of Engineering Technology (CTW)
Department of Mechanics of Solids, Surfaces & Systems
Chair of Nonlinear Solid Mechanics

Examination committee:

Chair head: prof. dr. ir. A. H. VAN DEN BOOGAARD
External member: prof. dr. ir. R. AKKERMAN
Supervisor: dr. ir. H. J. M. GEIJSELAERS
Daily supervisor: ir. G. T. HAVINGA

Enschede, The Netherlands, August 31, 2015

"Not all who wander are lost"

- J. R. R. Tolkien

Abstract

Production standards nowadays are continuously increasing. Therefore there is a call for thorough understanding of production processes and new methods of process control. One of these new methods of process control is by making use of a model based control scheme.

The goal of this work is to build a detailed, accurate and fast model of a bending process, which can be used for model-based control.

The bending process of interest is the plastic deformation of a 3 mm steel flap to an angle of 50° . This flap is part of a demonstrator product especially designed for the MEGaFIT (Manufacturing Error-free Goods at First Time) project in which the University of Twente en Philips cooperate closely.

Finite Element (FE) modeling is used to model the bending process. The output of the FE-model is a force curve similar to the force curve as measured in the bending process.

Proper Orthogonal Decomposition (POD) is used to reduce the result space from a series of FE analysis. Using a Radial Basis Function (RBF) a meta model is fit through this reduced result space.

With an average wall time of 0.03 s, the build PODRBF-model is fast enough to be used in an inverse analysis on which a model based control scheme can be designed. The PODRBF-model is detailed and accurate enough to estimate 3 parameters with 10 % accuracy.

Keywords: PROPER ORTHOGONAL DECOMPOSITION, RADIAL BASIS FUNCTIONS, INVERSE ANALYSIS, PARAMETER ESTIMATION

Preface

This thesis is written as a completion of the master Applied Mechanics at the University of Twente. When I started my bachelor Advanced Technology five years ago, I never expected to be where I am now. If somebody in high school told me that I would end up doing Mechanical Engineering, I would have laughed at him. However, during my bachelor I found out it were the courses on beam theory and mathematics I enjoyed specifically.

So, in September 2013 I started my master Applied Mechanics. It were the courses on numerical methods, computational optimization and non-linear solid mechanics I liked the most. During my internship in a production facility for diapers I found out another fascination of mine: production processes.

When I sought for a master's assignment I wanted to combine both interests. In a call with Timo Meinders he convinced me that this assignment wouldn't be so much programming and I decided to give it a shot. Well, I know better now.

In my first year as a bachelor student my programming skills were those from a student assistant. And by that, I mean that I wasn't programming myself. Looking back at the past 5 years, and the last 12 months specifically, I can say I have learned a lot. I have grown as a person and I would therefore like to take this opportunity to thank a few people who in some way contributed me in being able to do this.

Jos Havinga for all the input and all the support you gave to me in the past period. No matter how many times I knocked on your door, it was always open.

Haico Stegink for keeping patient with me. For all the times I was late for dinner and accepting our apartment was probably a little less clean last month. I know it wasn't easy all the time, but I must say I highly value the advice, time and love you always have for me.

Femke de Gooijer for being my lovely sister, for all the entertainment you brought to me during our hours in the gym or while having one, or one too many, beers. I really appreciate that you decided to start studying at the University of Twente as well. I am grateful to have you in my life.

Hendrik Spoelhof and the rest of the boys in N242 for all the thesis-related discussions and the less related conversations we had.

I hope one will enjoy reading this thesis as much as I enjoyed writing it.

Boukje Marije de Gooijer

Contents

Abstract	V
Preface	VII
Nomenclature	3
List of Abbreviations	4
1 Introduction	5
1.1 This work	5
1.2 The demonstrator product	5
1.3 Outline of this work	6
2 The production process	7
2.1 The bending module	7
2.2 The bending step	9
3 Modeling the bending step	10
3.1 Software	10
3.2 Geometry	10
3.3 Motion of the punch	12
3.4 Material model	12
3.5 Output of the FE-model	14
4 Parameter study	16
4.1 Parameters incorporated in the FE-model	16
4.2 Variation 1-by-1	17
4.3 Parameter space	21
5 Approximating the Finite Element Analyses	22
5.1 Proper Orthogonal Decomposition	22
5.2 Radial Basis Function	26
5.3 Force curves using a PODRBF approximation	28
5.4 Variation 1-by-1 using a PODRBF approximation	30
6 Inverse analysis	33
6.1 Weight Function	33
6.2 Error Function	34
6.3 Parameter estimation	36
7 Conclusion	46
8 Discussion & recommendations	47
8.1 Material model	47
8.2 Parameter space	47
8.3 POD basis	47
8.4 Inverse analysis	47
References	48
A Modeling in Marc Mentat	50
A.1 2D model	50
A.2 3D model	50
A.3 Contact modeling	51
A.4 Analysis	51

B	Parameter study (continued)	53
B.1	All parameters and their values	53
B.2	Force curves for less influential parameters	54
C	Parameter estimation	56

Nomenclature

A	Cross-sectional area [mm^2]
A_{jm}	Amplitude scalar of force curve m corresponding to j -th POD direction
E	Young's modulus [MPa]
$F(t_n)$	Force curve discretized in N time steps
L	Length [mm]
M	Number of force curves in snapshots matrix
N	Number of time steps in snapshot matrix
N_φ	Number of POD directions included in the truncated POD basis
T	Period of the punch motion [s]
$\bar{\Phi}$	Truncated POD basis
$\bar{\mathbf{A}}$	Truncated amplitude matrix
Φ	POD basis [Φ_{nj}]
φ_j	Vector containing the j -th POD direction
δ_{punch}	Final punch depth [mm]
$\dot{\epsilon}$	Strain rate [1/s]
γ	Spring constant [N/mm]
\hat{A}_j	Approximated amplitude scalar corresponding to the j -th POD direction
$\hat{\mathbf{F}}$	Vector containing an approximated force curve
$\hat{\mathbf{a}}$	Vector collecting the approximated amplitude scalars \hat{A}_j
λ	Eigenvalue
\mathbf{A}	Amplitude matrix [A_{jm}]
\mathbf{F}	Snapshot matrix [F_{nm}]
\mathbf{F}_m	Vector containing force curve m
\mathbf{a}_j	Amplitude vector corresponding to the j -th POD direction
\mathbf{a}_m	Vector containing the amplitudes corresponding to force curve m
\mathbf{v}	Eigenvector
$\mathbf{z}, \mathbf{z}_m, \mathbf{z}_p$	Point in parameter space \mathbf{Z}^D , indexed with m for the initial DOE and indexed with p for the validation set
ψ	Radial basis function in amplitude approximation
σ_y	Yield stress [MPa]
t_n	Time at point n [s]
w	Weight scalar in amplitude approximation

List of Abbreviations

DOE	Design Of Experiments
FE(M)	Finite Element (Method)
LHS	Latin Hypercube Sample
POD	Proper Orthogonal Decomposition
RBF	Radial Basis Function

1 Introduction

Ever increasing production standards demand for advanced methods of process control. Unfortunately, variations in process parameters are inevitable and, in the worst case, unmeasurable. These variations can have major influence on the outcome of the final product. Increasing production standards, such as decreasing tolerances and lower scrap rates, therefore call for thorough understanding of production processes and new methods of process control. One of these new methods of process control, is by making use of a model based control scheme.

1.1 This work

In this work the possibility of using model based control in a metal forming process is investigated. The work is done in contribution to the MEGaFiT (*Manufacturing Error-free Goods at First Time*) project in which the University of Twente and Philips cooperate closely. Within the MEGaFiT project a demonstrator product is designed to study the feasibility of inline process control. The production step of interest is a bending process in which a force curve is measured. Finite Element (FE) analysis will be used to model this production step. The force curves from the finite element analyses are used to gain insight into the influence of (un)measurable parameters. However, as the used FE-model generally takes 1000 seconds to generate a force curve this model is too slow to be used in a control scheme. The 10 most influential parameters are therefore used to build a new, faster model to approximate the force curve. The approximation is based on a Proper Orthogonal Decomposition (POD) combined with Radial Basis Functions (RBF). This PODRBF-model can be used in an inverse analysis on which a control scheme can be based.

The goal of this work is to build a detailed, accurate and fast model of the bending stage, which can be used for model-based control.

1.2 The demonstrator product

A top and side view of the demonstrator product as designed for the MEGaFiT project can be found in Figure 1.1. The product is specially designed to study the feasibility of inline process control, therefore there are no specified requirements. The three flaps are bend to an angle of 50° . During this bending step a force curve is measured, as can be found in Figure 1.2a. The three force curves measured upon bending the three flaps differ from flap to flap, as well as per product.

In Figure 1.2b the angle measurement per product of the right most flap can be found. The angle measurement is done after the product obtains its final geometry. As one can see the angles display high frequent variation which is difficult to control with direct feedback [7]. The angle measurements are therefore not suitable to be used in a control algorithm. In this work it is studied if the force curves can be used instead.

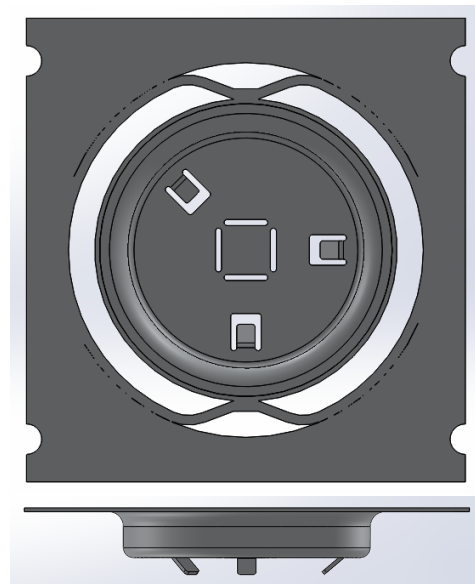
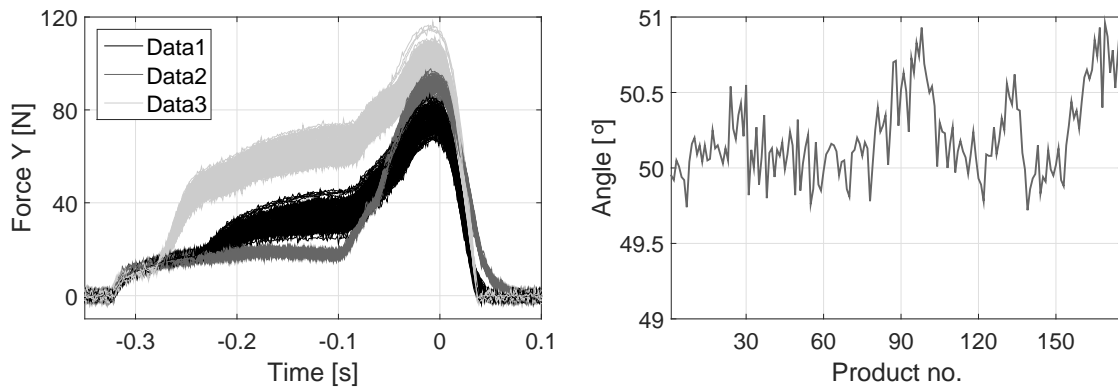


Figure 1.1: Top and side view of the demonstrator product.



(a) Force curves of the 3 flaps versus production time. (b) Angles of the rightmost flap versus product number.

Figure 1.2: Force curves and angles from 176 demonstrator products as measured in the test setup.

1.3 Outline of this work

The production process of the demonstrator product is described in section 2. How the bending step of in this production process is modeled using finite elements is described in section 3. The main output of the FE-model is a force curve similar to the one as presented in Figure 1.2a.

In Figure 1.3 the further outline of this work is presented. In section 4 it is described how the FE-model is used to do a parameter study. The parameter study is done to find the most influential parameters. By comparing the force curves from the FE-model with the force curves as measured in the test setup the 10 most influential parameters are chosen. Using these 10 most influential parameters a parameter space is defined in which an initial design of experiments is chosen. The sets of input parameters in the initial design of experiments (\mathbf{z}_m) are used as input for a new series of finite element simulations.

The force curves from this new series of FE-analyses ($F_{\text{FEM}}(\mathbf{z}_m)$) are used as input in a Proper Orthogonal Decomposition (POD). Section 5.1 describes how the force curves are approximated using POD. In section 5.2 it is presented how Radial Basis Function (RBF) are used to go from a discrete input (\mathbf{z}_m) to a continuous one (\mathbf{z}). From this a force curve based on any combination of input parameters ($F_{\text{PODRBF}}(\mathbf{z})$) can be approximated in a fast way.

Combining this fast approximation with experimental results (F_{exp}) is the key to an inverse analysis (section 6). In this inverse analysis an error function ($e(\mathbf{z})$) is minimized to estimate the combination of input parameters (\mathbf{z}). In section 6.3 the results of a parameter estimation are presented.

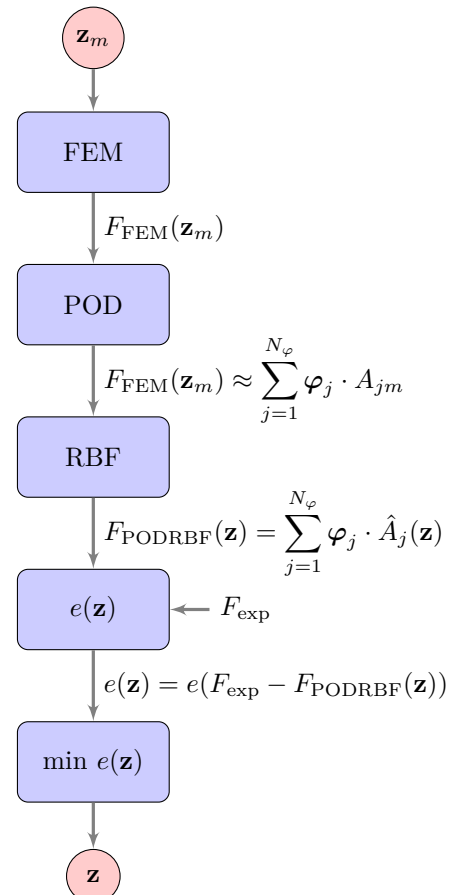


Figure 1.3: Flow diagram to present outline of this work.

2 The production process

The production process of the demonstrator product is divided in four different modules. Figure 2.1 shows a picture of the production line. The product moves in one long strip through four modules from left to right in the picture. The production speed can range from 12 rpm up to 60 rpm and is the same in each module. In this work the focus is on production with 12 rpm. From the left to the right in Figure 2.1 the modules are *Cutting*, *Deep-Drawing*, *Coining* and lastly *Bending*. The possibilities in using model-based control are investigated for the bending module. Therefore this section elaborates specifically on that module.



Figure 2.1: Test setup for production of the demonstrator product as used in the MEGaFit project.

2.1 The bending module

The bending module consists of six production steps. A cross-sectional view of the bending module can be found in Figure 2.3. The corresponding demonstrator product in each step can be found in Figure 2.4.

The first step is the entry of the product in the module. In the second step (2.4a, Detail A in Figure 2.3) the three so-called flaps are cut. The rightmost flap is in longitudinal direction, clockwise the next flap is in lateral direction and the last flap is under an angle of 135° with both other flaps.

After cutting, the flaps are bend to an angle of 50° (2.4b, Detail B in Figure 2.3). During this step the bending force of all three flaps is measured. An example of the measured force curves can be found in Figure 1.2a.

After bending the flaps, the flaps are bent back as desired (2.4c, Detail C in Figure 2.3). The extend to which the flaps are bent back can be regulated per product and per flap.

In the last step of the module (2.4d, Point D in Figure 2.3) a picture of the flap in longitudinal direction is captured. From the picture the angle can be calculated with an accuracy of $\pm 0.1^\circ$. As processing the image takes some time the information on the final angle of product N is only available when product $N+2$ or even $N+3$ is being produced.

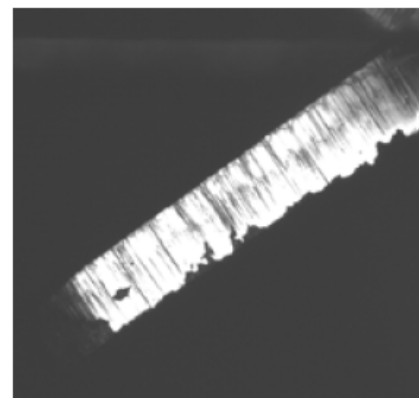
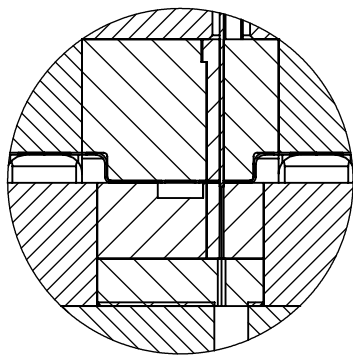
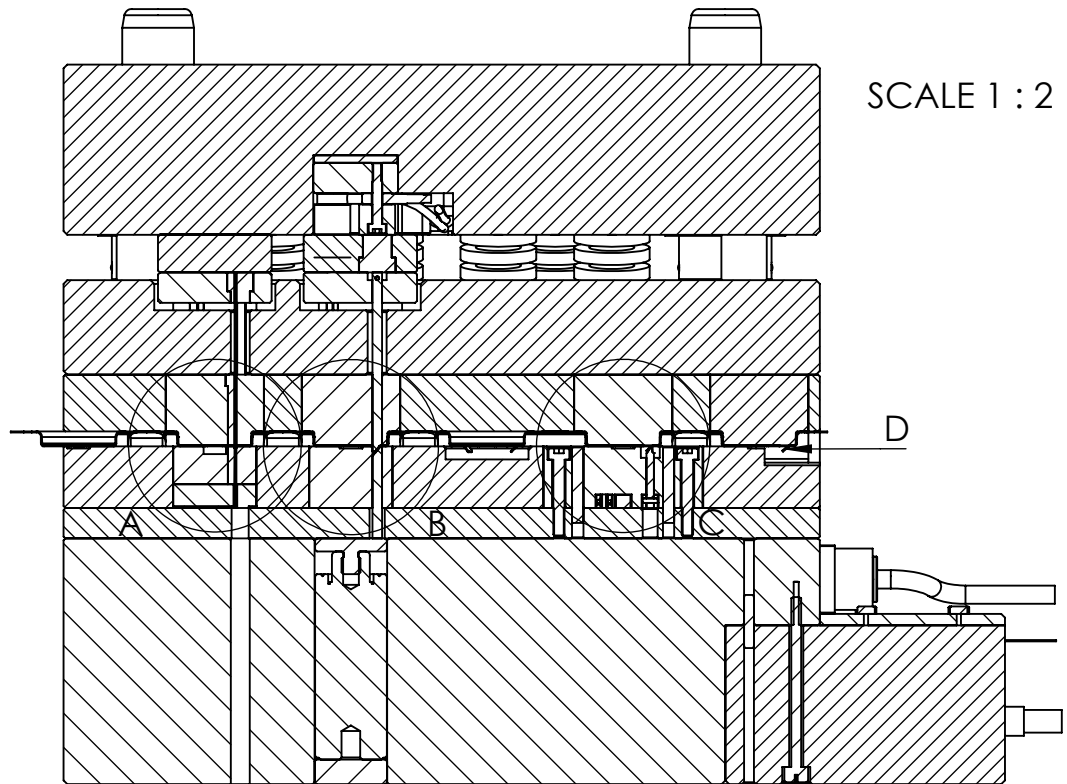
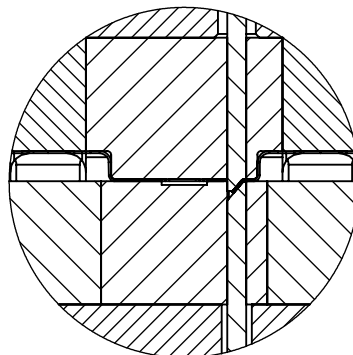


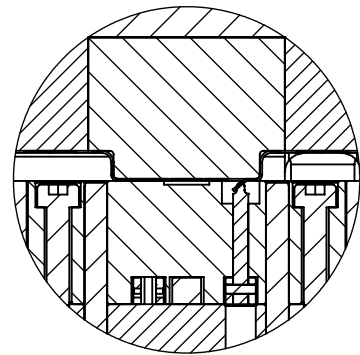
Figure 2.2: Picture of the flap as taken in the test setup (Point D in Figure 2.3).



DETAIL A
SCALE 1 : 1

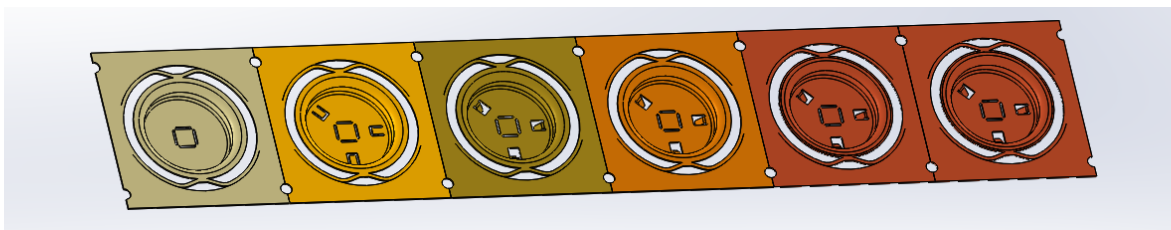


DETAIL B
SCALE 1 : 1



DETAIL C
SCALE 1 : 1

Figure 2.3: Cross-sectional view of the bending module with close-ups of the different production steps.



(a) Cutting
(Detail A)

(b) Bending
(Detail B)

(c) Back bending
(Detail C)

(d) Angle measurement
(Point D)

Figure 2.4: Demonstrator product in the bending module at different production steps.

2.2 The bending step

As the force curve is measured in Detail B in Figure 2.3, this section elaborates on that bending step specifically. The most important parts involved in the bending step are denoted in Figure 2.5. All parts above the product belong to the *upper part* of the module, whereas all the parts below the product belong to the *lower part* of the module.

The upper part of the module is connected to a Bruderer stamping press. The movement induced by the stamping press is denoted with *Crank drive* in Figure 2.5. The entire upper part moves downwards until the *blank holder* clamps the product. Thereafter the blank holder guides the further downward movement of the *punch*. The movement is characterized by a Crank curve as described in more detail in section 3.3. Above the punch a *force sensor* is placed. This force sensor does not measure negative forces as can be seen clearly in Figure 1.2a.

The lower part of the module is fixed, except for the *die* which is connected to a *gas spring*. The *punch* and *die* together bend the *flaps* in the product to an angle of 50° .

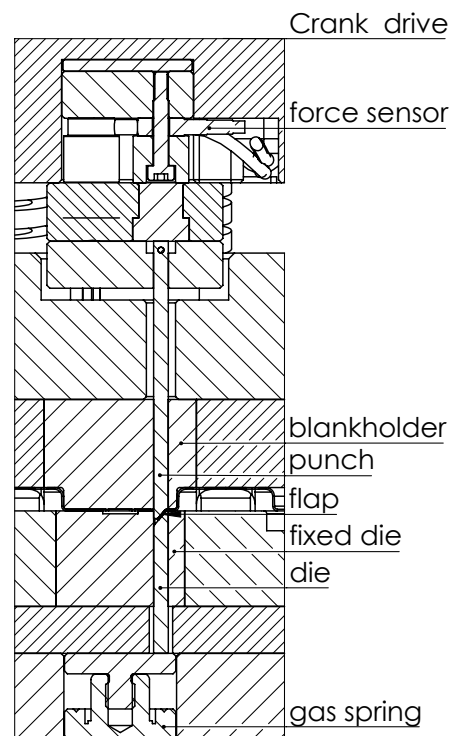


Figure 2.5: Cross-sectional view of the bending step with most important parts involved.

3 Modeling the bending step

Probably the hardest part in any finite element analysis is representing the real world in a satisfying way. In this section it is described how the bending step as presented in section 2.2 is modeled using finite elements.

The more elaborated a model becomes, the more expensive. By calling a model *expensive* one means that it costs a lot of computational power or time to find a solution. The objective is to model the bending step in the cheapest way without compromising too much on the behavior as seen in reality.

A compromise in modeling the real world is already made by focusing only on the third step of the bending module instead of on the total production process. One can imagine that previous production steps can have major influence on the behavior of the product in the bending step. For example deep-drawing can have major influence on the material properties in different directions. However, to lower the computational costs the historical information of the process is completely neglected.

3.1 Software

The bending step is modeled using the FE software MSC Marc 2013.1. A preprocessor called Mentat is used to generate the Marc-input files (.dat). To manage the input and output for the finite element analysis MathWorks' MATLAB is used. In MATLAB the different input files (.proc) for the preprocessor are generated. The output file generated by Marc (.sts, .t16) are handled in MATLAB as well. The informational flow between the different programs can be found in Figure 3.1. More information on the settings used in Marc Mentat can be found in Appendix A.

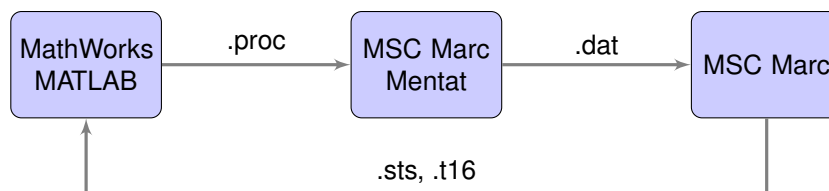


Figure 3.1: Information flow between different programs.

3.2 Geometry

A snapshot of the FE-model with several indicated 'parts' can be found in Figure 3.2. The following parts can distinguished:

- flap,
- punch,
- die,
- spring 1 & spring 2,
- crank drive ($H(t)$),
- blank holder,
- fixed die.

The most important part is the *flap*. The flap is modeled with 3000 fully integrated bilinear rectangular elements. In the remainder of this work flap and sheet are used interchangeably. The mesh of the flap is finest around the bending area. To decrease numerical noise, no mesh-refinements are done. The material behavior of the flap is modeled using a strain rate dependent material model. The strain rate sensitivity is modeled using a power law as described more elaborately in section 3.4.

Both the *punch* and the *die* are modeled with fully integrated bilinear triangular elements, 1082 and 266 elements respectively. To reduce computational time only the lower part of the punch and the upper part of the die are modeled. To take into account the elasticity of the part of tooling which is cut off, the punch and die are both connected to a spring. The top of the punch is connected to *spring 1*,

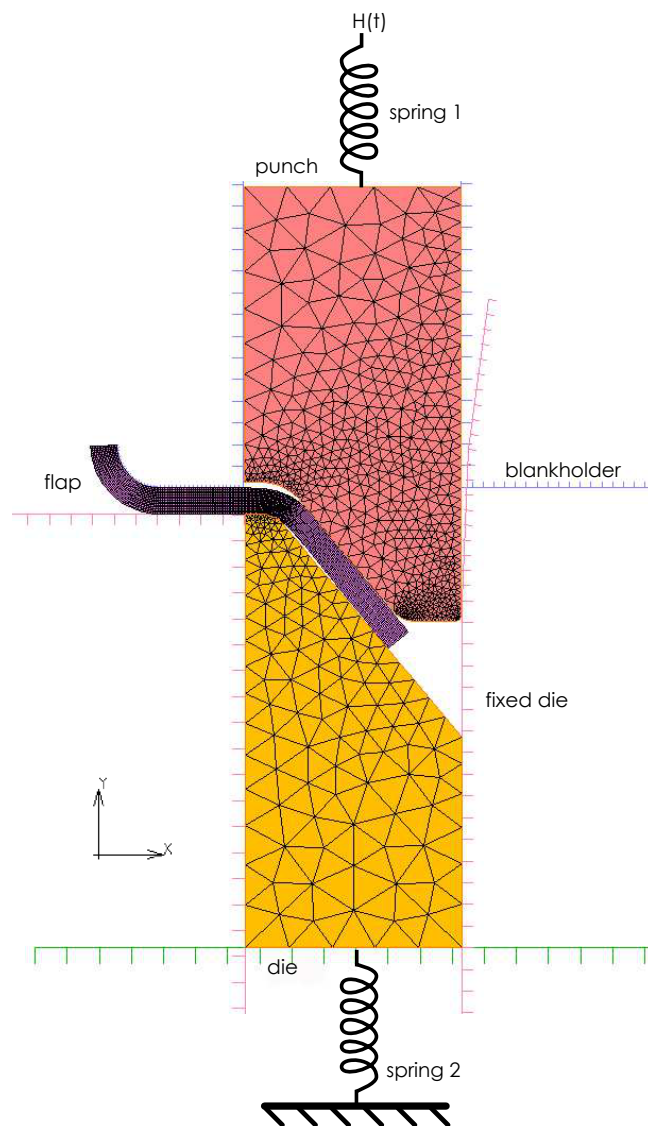


Figure 3.2: Two-dimensional model in Mentat.

whereas bottom of the die is connected to spring 2. The spring constant (γ) for both springs can be calculated as follows.

$$\gamma = \frac{AE}{L} \quad (3.1)$$

Herein A is the cross-sectional area of the replaced part, E the Young's modulus of the material and L the length of the replaced part.

The punch movement is described by a Crank curve ($H(t)$). How this movement is implemented in the FE-model is described in section 3.3.

To reduce computational time the *blankholder* and *fixed die* are modeled as rigid bodies. These rigid bodies have no elasticity, and thus cannot deform. On the other hand, the friction between a rigid body and a deformable body is modeled. Note that the geometry of the fixed die in the FE-model differs a lot from the geometry as in Figure 2.2. When building the model it was encountered that the initial contact between a node of the punch with the fixed die gave large peaks in the y -component of the contact force. To smooth out these numerical errors the fixed die is modeled with a fillet with large radius instead of a 90° angle.

3.3 Motion of the punch

The motion of the punch is prescribed at the upper node of spring 1 (see Figure 3.2). The travel distance of the punch from its initial position ($H(t)$ in mm) is described by a Crank curve. To set the desired punch depth, the final punch depth (δ_{punch}) is subtracted from the travel distance $H(t)$.

$$H(\alpha) = KR \cdot \left[1 - \cos(\alpha) + \frac{1 - \sqrt{1 - \lambda^2 \sin^2(\alpha)}}{\lambda} \right] - \delta_{\text{punch}} \quad (3.2)$$

with $K = 0.6035$ a ratio between the two main levers, R the eccentric radius (31.45 mm), α the Crank angle in radians and $\lambda = 0.0850$ a ratio between the length of the connecting rod and the eccentric radius as provided by Bruderer, the manufacturer of the stamping press.

The travel distance as a function of the Crank angle is rewritten to a function of time. To align the curves at the deepest point on $t = 0$ a shift in Crank angle $\Delta\alpha$ is introduced.

$$H(t) = KR \cdot \left[1 - \cos\left(\frac{2\pi t}{T} - \Delta\alpha\right) + \frac{1 - \sqrt{1 - \lambda^2 \sin^2\left(\frac{2\pi t}{T} - \Delta\alpha\right)}}{\lambda} \right] - \delta_{\text{punch}} \quad (3.3)$$

with T the period of the punch motion. The period for a production speed of 12 rpm is 5 s. The resulting punch movement for several punch depths is plotted in Figure 3.3. Note the difference in initial time of contact (t_0) due to the different final punch depths.

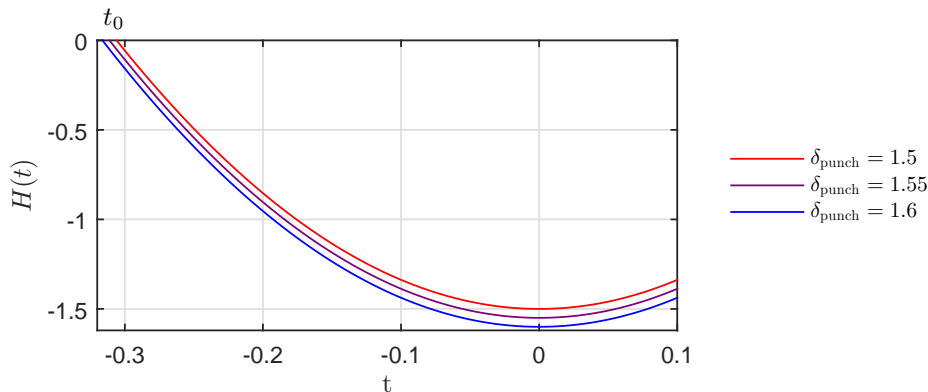


Figure 3.3: Crank curve for different punch depths (δ_{punch}) and the influence on time of initial contact (t_0).

3.4 Material model

The material of the product and thus the flap is AISI420 steel. To model the bending process isotropic material behavior is assumed. This means that the material is assumed to react the same in different directions. As a result the FE-model can be compared to the measured force curves from the test setup of all three flaps.

The flap is deformed plastically. To determine if plastic deformation occurs the Von Mises yield criterion is used.

$$\sigma_y = \sqrt{\frac{1}{2} [(\sigma_{11} - \sigma_{22})^2 + (\sigma_{22} - \sigma_{33})^2 + (\sigma_{33} - \sigma_{11})^2 + 6(\sigma_{12}^2 + \sigma_{23}^2 + \sigma_{31}^2)]} \quad (3.4)$$

The plastic behavior of the material is modeled using experimental data. The strain rate sensitivity of the material is based on extrapolated data curves [3]. The extrapolated yield-curve for zero strain rate ($\dot{\epsilon}_{\text{extra}}^p = 0$) can be found in Figure 3.4. To model the strain rate dependency a so-called power law is used. This yield-curve at zero strain rate $\sigma_y(\epsilon | \dot{\epsilon} = 0)$ is multiplied with an exponential function.

$$\sigma_y(\epsilon, \dot{\epsilon}) = \sigma_y(\epsilon | \dot{\epsilon} = 0) \cdot \left(1 + \left(\frac{\dot{\epsilon}}{10^{c_1}} \right)^{c_2} \right) \quad (3.5)$$

Herein $\dot{\epsilon}$ is the strain rate, and c_1 and c_2 are material constants.

In Figure 3.6 snapshots of the FE-model at various moments in time are displayed. The colors represent the equivalent plastic strain rates. The maximum equivalent strain ($\varepsilon_{\text{eq}}^p$) and the maximum equivalent strain rate ($\dot{\varepsilon}_{\text{eq}}^p$) reached in the FE-model using nominal settings are slightly over 0.5 and 5/s respectively. The maximum strain rate reached in the experiments ($\dot{\varepsilon}_{\text{exp}}^p$) is 0.2/s. The values for c_1 and c_2 used in modeling the bending step are thus strongly extrapolated.

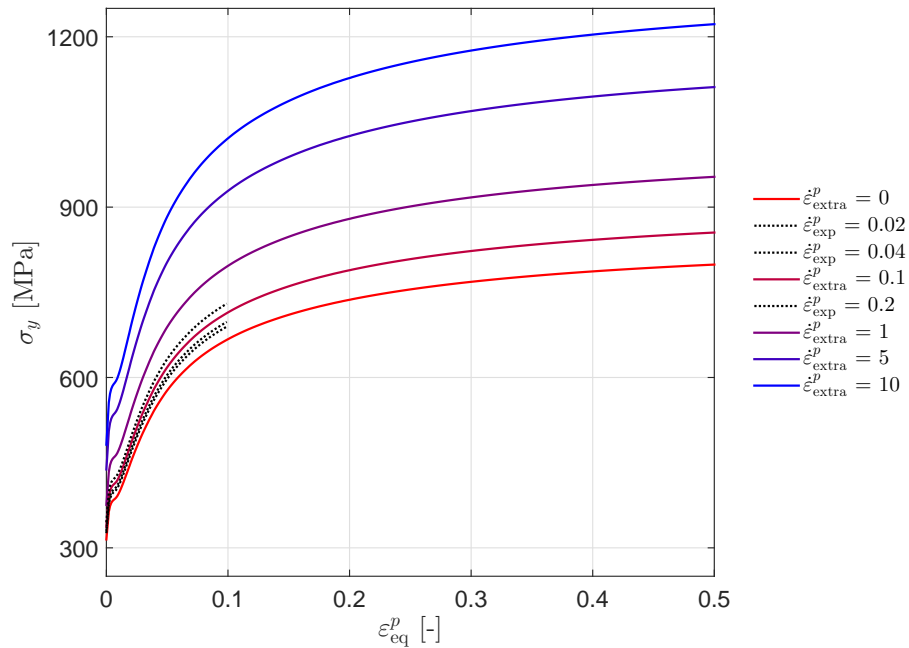


Figure 3.4: Equivalent plastic strain versus the yield stress for experimental data ($\dot{\varepsilon}_{\text{exp}}^p$) and extrapolated data ($\dot{\varepsilon}_{\text{extra}}^p$). Material constants used in the extrapolation are $c_1 = 1.63$ and $c_2 = 0.44$.

3.5 Output of the FE-model

Among other things the output file of the FE-model contains the force each contact body experiences over time as well as the positions of all nodes. MATLAB is used to store both the force curve of interest and the final angle of each simulation.

Force curve

Only the y -component of the force as experienced by the punch is used for further analysis. The force curve from the FE model, as plotted in Figure 3.5, contains a few characteristics.

At t_0 the punch makes its initial contact with the flap. This initial position of the punch is displayed in Figure 3.6a. Depending on the final punch depth (δ_{punch}) the time at which this initial contact takes place can differ (see Figure 3.3). From t_0 to t_1 the flap is bend without any restrictions, this is called the *free bending* stage and is displayed in Figure 3.6b.

At t_1 there is an abrupt change in slope because the contact area starts to move. This change in contact area can be seen clearly when comparing Figure 3.6b and Figure 3.6c.

At t_2 the flap makes contact with the die as displayed in Figure 3.6d. This again causes an abrupt change in slope. At $t = 0$ the punch reaches its maximum depth. Between t_2 and $t = 0$ the flap is flattened. Within this *flattening* stage the punch experiences its maximum force at t_3 . The FE-model at maximum force is displayed in Figure 3.6e. The maximum force is not reached when the punch reaches its deepest point due to the strain rate sensitivity of the material.

After the punch reaches its deepest point it starts to move upward. Due to a phenomena called springback the flap moves a bit upward as well. The deformation of the flap after springback can be found in Figure 3.6f.

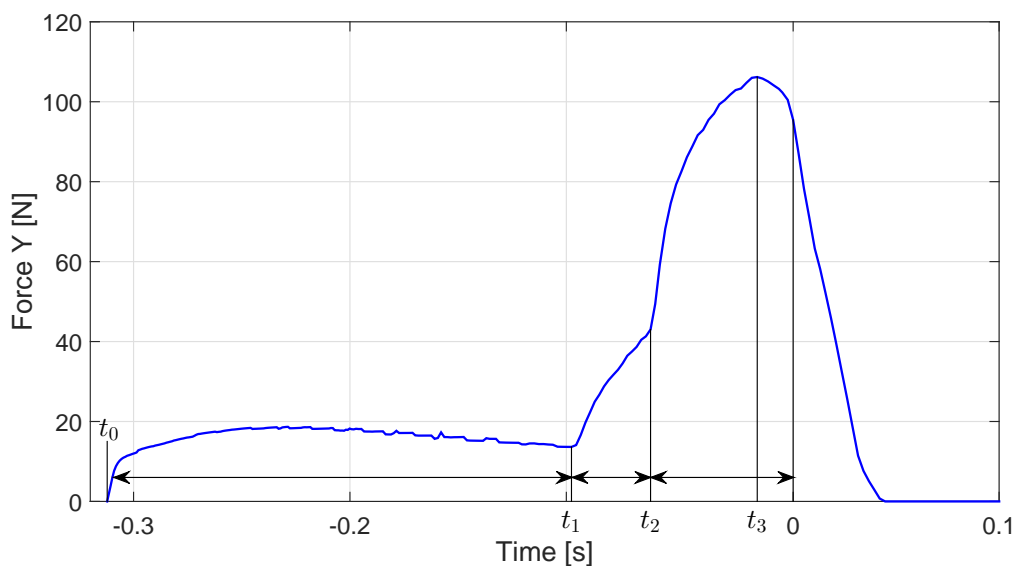


Figure 3.5: Force curve with different characteristics.

Final angle

The calculation of the angle of the flap is based on the difference between the initial and final position of two nodes. The nodes on which the calculation is based are taken sufficiently far away from the bending area. A closeup of flap and the used nodes can be found in the Figure A.1 in Appendix A.

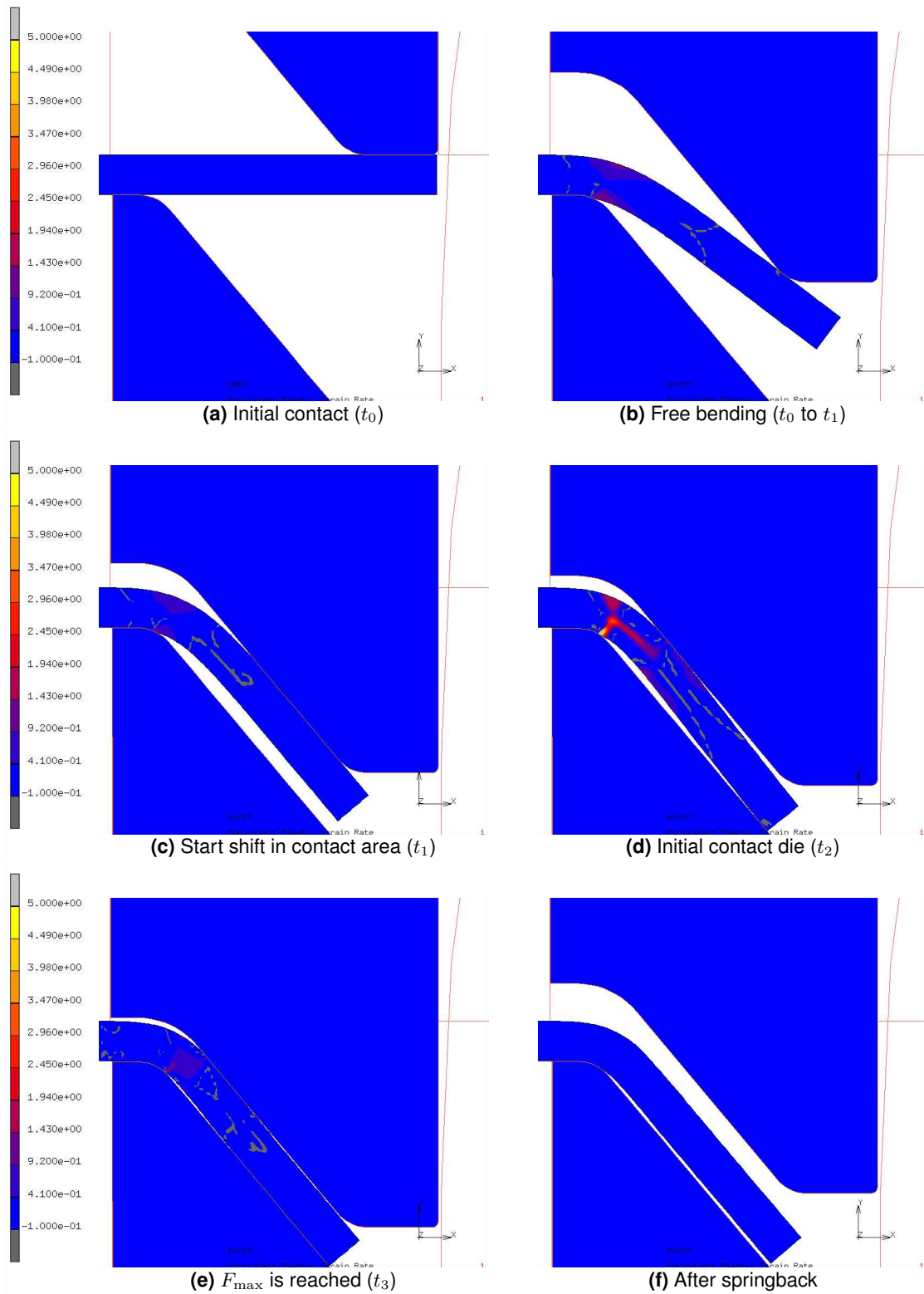


Figure 3.6: Snapshots of finite element analysis at different times. Color represents the equivalent plastic strain rate.

4 Parameter study

In this section all parameters incorporated in the FE-model are described. By means of a 1-by-1 variation the influence of these parameters is screened. Based on this screening the 10 most influential parameters are presented in section 4.2. By examining the differences between the FE-model and the experimental data the ranges for some parameters are reduced. Based on the reduced ranges a parameter space is build and presented in section 4.3.

4.1 Parameters incorporated in the FE-model

For convenience the parameters are divided in four groups namely *alignment*, *material*, *geometric* and *numerical*. All parameters incorporated in the FE-model and their used values can be found in Appendix B Table B.1. All parameters are varied around a nominal setting.

Alignment parameters

The degrees of freedom with which each part is modeled are depicted in Figure 4.1. The left part of the blank holder is chosen as a reference for the x -alignment. For the y -alignment the position of the fixed die is chosen as a reference. The clearance between the punch and the blank holder is chosen to be equal on both sides. The same holds for the clearance between the die and the fixed die. The x -alignment of the lower part is defined as the difference between the center lines of the punch and the die. An overview of the most important alignment parameters can be found in Table 4.1.

Note that by changing the sheet length and the sheet thickness the mesh of the flap changes as well. The number of elements stays the same, however their width and height changes.

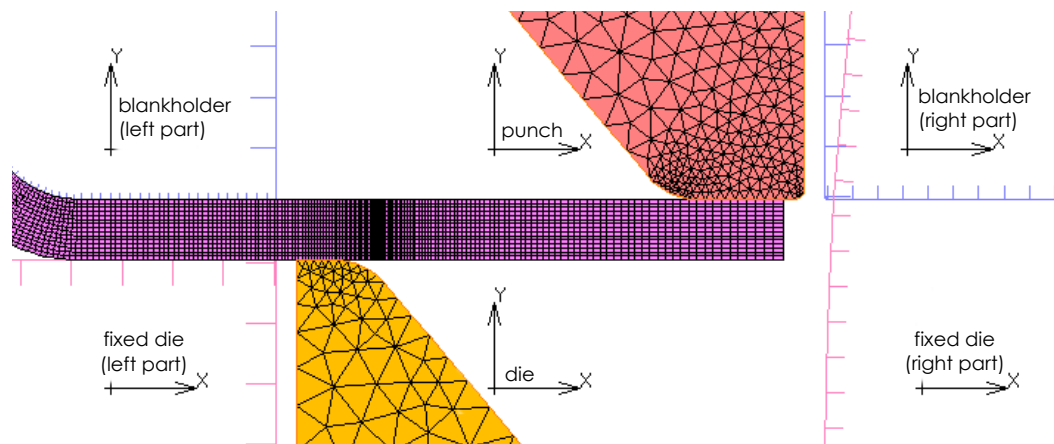


Figure 4.1: Degrees of freedom for different parts.

Table 4.1: Alignment parameters in FE-model with corresponding minimum, maximum and nominal values.

Alignment parameter	min	nominal	max	unit
clearance punch/blankholder (x -alignment)	0	0.0025	0.005	mm
clearance die/fixed die (x -alignment)	0	0.002	0.004	mm
x -alignment lower part (die & fixed die)	-0.0195	0.0005	0.0205	mm
sheet length (x -alignment cutting)	-0.2	0	0.01	mm
sheet thickness (y -alignment upper part)	0.29	0.3	0.31	mm
y -alignment die	-0.02	0	0	mm
punch depth (δ_{punch} , y -alignment punch)	1.5	1.56	1.6	mm
blankholder force (y -direction)	-50	-300	-500	N
sheet width (z -direction)	1.4	1.5	1.6	mm

Material parameters

As only the bottom of the punch is modeled, the removed elasticity is compensated with a spring. The length of the punch head which is modeled (L_{head}) is 5 mm. The total length of the punch (L_{tot}) as found in the SolidWorks model is 47.3 mm. The Crank drive (L_{drive}) is not directly connected to the top of the punch, but 2 mm below (Figure 2.3). The length of the removed part of the punch can therefore be written as:

$$L = L_{\text{tot}} - (L_{\text{head}} + L_{\text{drive}}) = 40.3 \text{ mm} \quad (4.1)$$

The cross-sectional area of the punch of 4.97 mm^2 is derived from the SolidWorks model as well. With a Young's Modulus of $E = 210 \times 10^3 \text{ GPa}$, the nominal spring stiffness (γ_1) of the spring connected to the punch (spring 1) can be calculated using equation 3.1. Hence, the nominal spring stiffness of the punch is $25\,898 \text{ N/mm}$.

The nominal spring stiffness (γ_2) of the spring connected to the die (spring 2) is calculated in the same manner. With $L_{\text{tot}} = 24.3 \text{ mm}$, $L_{\text{head}} = 5 \text{ mm}$ and $L_{\text{drive}} = 0 \text{ mm}$, the length of the removed part of the die is $L = 19.3 \text{ mm}$. With a Young's Modulus of $E = 210 \text{ GPa}$ and a cross-sectional area of $A = 4.97 \text{ mm}^2$, the nominal spring stiffness of the die is calculated to be $54\,078 \text{ N/mm}$.

An overview of the most important material parameters can be found in Table 4.2.

Table 4.2: Material parameters in FE-model with corresponding minimum, maximum and nominal values.

Material parameter	min	nominal	max	unit
Poisson ratio	0.29	0.3	0.31	-
Young's modulus (E)	190	210	230	GPa
sheet yield stress premultiplier	0.9	1	1.1	-
c_1 strain rate dependent model	1	1.63	5	-
c_2 strain rate dependent model	0.1	0.44	1	-
spring stiffness punch (γ_1)	1000	25898	35000	N/mm
spring stiffness die (γ_2)	40000	54078	60000	N/mm
friction coefficient	0	0.13	0.2	-

Geometric parameters

The fillet radius of the fixed die which is used to smooth the numerical errors in the y -component of the contact force, is varied between 10 and 50 mm.

Numerical parameters

The numerical parameters are only varied to find the right settings for the final model in MarcMentat. More on modeling in MarcMentat can be found in Appendix A.

4.2 Variation 1-by-1

All parameters are varied 1-by-1 between their minimum and maximum value to find their influence on the nominal force curve. In a screening all force curves are examined by eye judgment and the 10 most influential parameters are chosen and presented below. Figure 4.3 displays the forces curves based on the 10 most influential parameters, all force curves based on less influential parameters can be found in Appendix B Figure B.1. Based on a comparison with the force curves as measured in the test setup the minimum and maximum values for some parameters are changed.

Clearance die/fixed die

In Figure 4.3a the clearance between the die and the fixed die is varied as input in the FE-model. A smaller clearance gives rise to a larger maximum force, this particularly holds for the flattening stage and the maximum force. This is due to the fact that the die is more free to move with large clearances. The distance with respect to the axis of rotation of the flap becomes larger resulting in a smaller force needed to bend the flap.

X-alignment lower part

The x -alignment of the lower part has a large influence on the force curve, specifically in timing. As can be seen in Figure 4.3b a negative misalignment causes the contact area to change earlier. This is due to the fact that with large negative misalignment the punch is in contact with the fixed die. The fixed die forces the punch to the negative x -direction initiating the change in contact area earlier. Both a negative and positive misalignment cause a larger force in the flattening stage with respect to the nominal force curve. The positive misalignment causes the distance with respect to the axis of rotation of the flap to decrease. The negative misalignment has a larger impact on the maximum force than the positive misalignment, due to the contact with the fixed die. The slope after the maximum force is much steeper for negative misalignment, this is due to the friction with the fixed die.

Sheet thickness

The force curves based on changing the sheet thickness in the FE-model are plotted in Figure 4.3c. Generally a larger sheet thickness means a larger force. There is also a slight change in timing due to the change in punch depth. By evaluating the force curves from the test setup (Figure 1.2a) the choice is made to change the minimum and maximum values for the sheet thickness to 0.295 and 0.305 mm respectively.

Y-alignment die

The y -alignment of the die has a large influence, specially in timing as can be seen in Figure 4.3d. A negative misalignment causes a different curvature at the start of the free bending stage as there is no contact with the tip of the die initially. The time at which the contact area starts to change and the time at which the contact with the die takes place both shift in positive direction with negative misalignment. Generally a negative alignment means less force needed to bend the flap. In the experimental force curves the peak in the force curve is generally seen wider, than in the FE-model. Therefore the choice is made to set the minimum y -alignment of the die to -0.01 mm.

Punch depth

In Figure 4.3e the influence of changing the punch depth in the FE-model can be found. The most important effect is the change in maximum force. The force curve based on minimum punch depth is not found as such in the force curves from the test setup. Therefore the minimum punch depth is increased to 1.52 mm in the parameter space. The opposite holds for the maximum punch depth, this value is decreased to 1.58 mm. As the punch depth gets smaller, the product is processed in less time. This can be seen clearly in the timing of the force curve. With smaller punch depths the initial contact between the punch and the flap (t_0) is later. The initial contact between the die and the flap becomes later as well. With the minimum punch depth (1.5 mm) the flattening stage is not reached at all, hence there is no contact with the die. A larger punch depth initiates the shift in contact area earlier.

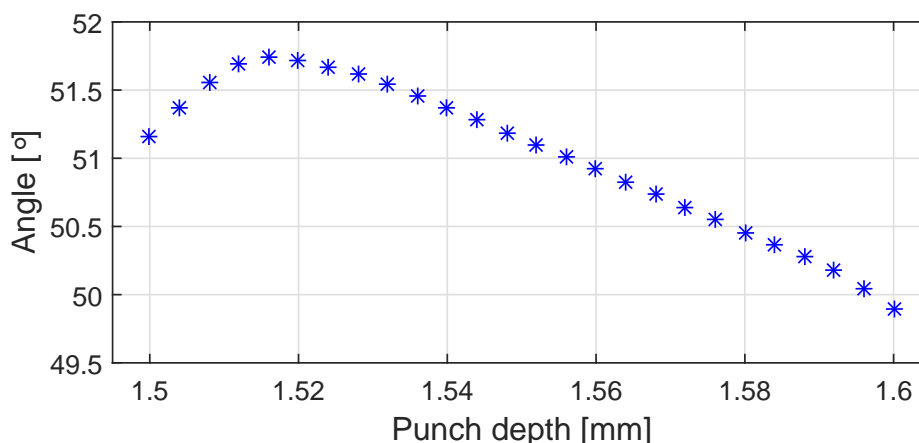


Figure 4.2: Final angle versus punch depth from the FE-model.

To check the numerical noise of the FE-model [8] the final angles corresponding to a wide range of punch depths are plotted in Figure 4.2. The largest angle is established with a punch depth of 1.516 mm. As can be seen in Figure 4.3e this is between the two force curves based on the smallest punch depths. This transition from an increasing final angle to a decreasing final angle has probably to do with the initial contact of the die. For a punch depth of 1.524 mm this stage is entered, whereas with the minimum punch depth this stage is not reached at all.

Sheet yield stress premultiplier

Generally a larger yield stress premultiplier means a larger force as can be seen in Figure 4.3f. Only after $t = 0$ there is a slight change in timing.

C₁ strain rate dependent model

In Figure 4.3g the force curves with varied material constant c_1 can be found. A smaller c_1 gives a larger force in all stages. Looking at equation 3.5 a smaller c_1 means the yield stress becomes higher. Hence, there is more resistance against deformation. This corresponds with the earlier initiation of the change in contact area for smaller c_1 . The maximum value for c_1 is decreased to 3 after examining various combinations of c_1 and c_2 . Both material parameters are used in the parameter space as their values are strongly extrapolated from the experimental results.

C₂ strain rate dependent model

A smaller c_2 gives a larger force in all stages as can be seen in Figure 4.3h. Again looking at equation 3.5, a smaller c_2 means a larger yield stress as

$$\lim_{c_2 \rightarrow 0} \left(\frac{\dot{\epsilon}}{10^{c_1}} \right)^{c_2} = 1.$$

With $c_2 = 0.1$ the FEA did not converge. The minimum and maximum values of c_2 are changed to 0.3 and 0.7 respectively.

Spring stiffness punch

The minimum value used as input for the spring stiffness of the punch is rather low. This is chosen as such to take into account the possible compliance of the machinery. As can be seen in Figure 4.3i a lower spring stiffness produces a wider, but lower peak. As can be seen in Figure 4.3i the force curve based on the maximum spring stiffness (35 000 N/mm) does not differ much from the force curve based on the nominal value for the spring stiffness (25 898 N/mm). Therefore the maximum value for the spring stiffness of the punch is reduced to slightly above the nominal value (26 000 N/mm).

Friction coefficient

Initially the friction coefficients between the punch and blank holder and between the die and fixed die, were varied separately from the friction coefficient between the tooling and the sheet and the friction coefficient between the punch and the fixed die. All friction coefficients have roughly the same influence as can be seen when comparing Figure 4.3j with Figure B.1k and B.1l in Appendix B. As the influence on the force curve is the same for all friction coefficients the choice is made to vary all friction coefficients at once in the parameter space.

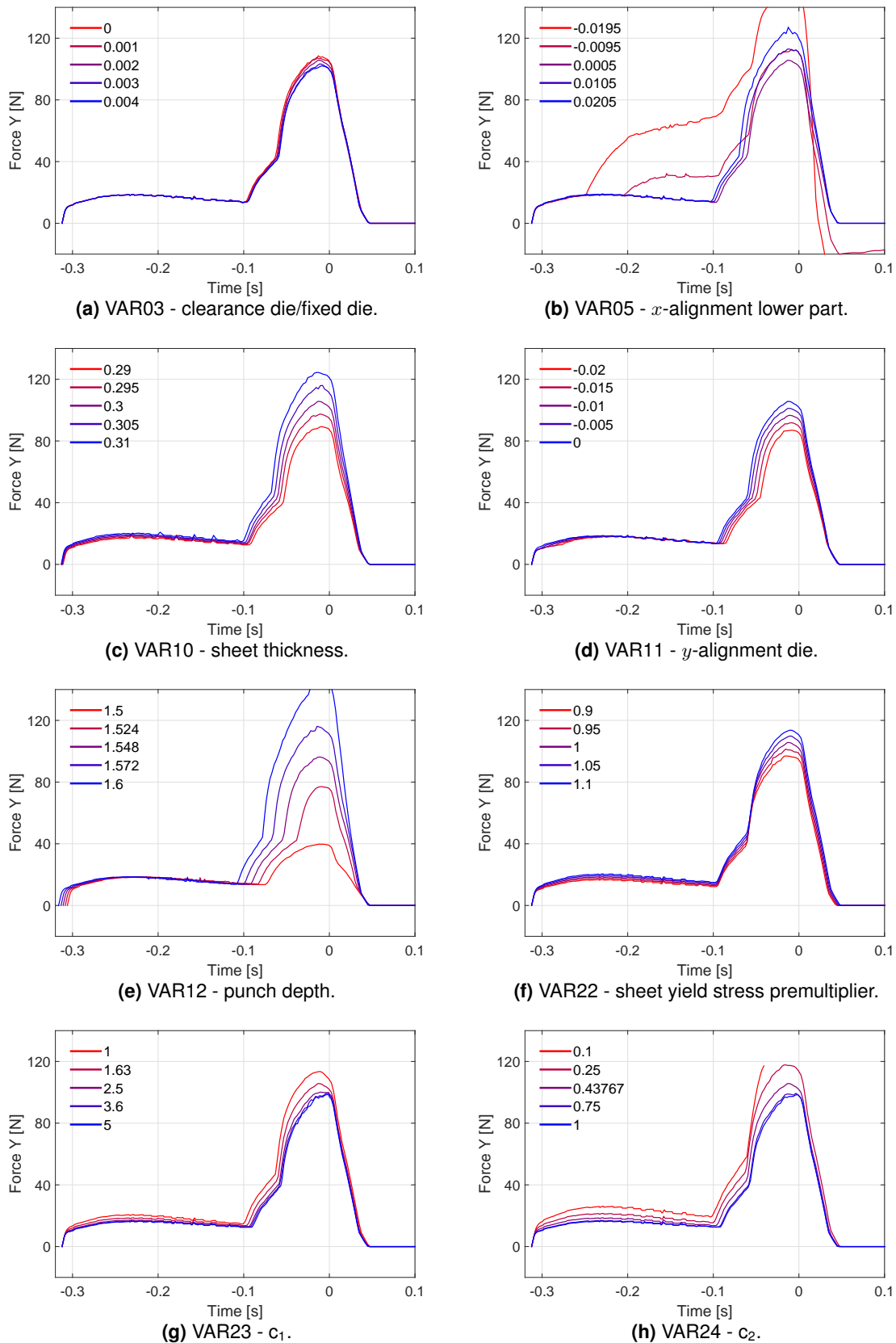


Figure 4.3: FEM curves for most influential parameters.

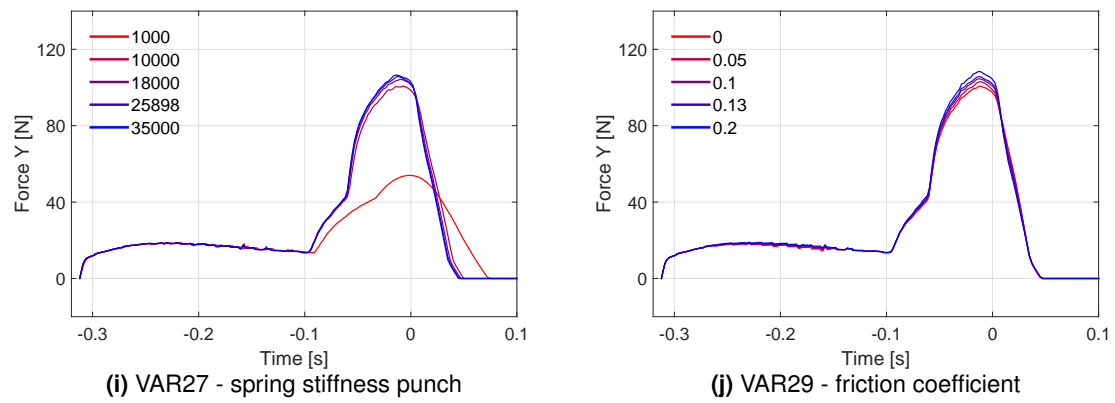


Figure 4.3: FEM curves for most influential parameters (cont.).

4.3 Parameter space

The 10 most influential parameters from the screening described in the previous section are used to define a parameters space (\mathbf{Z}^D). In Table 4.3 an overview is given from the new minimum and maximum values based on the screening. These minimum and maximum values are the minima and maxima of the real interval ($\mathbf{Z}^{(d)}$) on which each parameter ($z^{(d)}$) is defined. Hence, $D = 10$, and a point in the parameter space can be defined as:

$$\mathbf{z} = \{z^{(1)}, z^{(2)}, \dots, z^{(10)}\} \in \mathbf{Z}^D \quad (4.2)$$

Comparing Table B.1 and Table 4.3 one can see that by means of the screening the variables in the FE-model are reduced from 23 to 10. Only the alignment and material parameters are used in the parameter space.

Using a Latin Hypercube Sample (LHS), 4960 points in the parameter space were generated as an initial Design Of Experiments (DOE). Each point from the initial DOE (\mathbf{z}_m) is used as input for a new set of finite element analyses.

Table 4.3: Minimum and maximum values for selected variables used to define the parameter space.

Variable	Description	$\min(\mathbf{Z}^{(d)})$	$\max(\mathbf{Z}^{(d)})$	unit
Alignment				
$z^{(1)} = \text{VAR01}$	clearance die/fixed die	0	0.004	mm
$z^{(2)} = \text{VAR05}$	x -alignment lower part (die & fixed die)	-0.0195	0.0205	mm
$z^{(3)} = \text{VAR10}$	sheet thickness	0.295	0.305	mm
$z^{(4)} = \text{VAR11}$	y -alignment die	-0.01	0	mm
$z^{(5)} = \text{VAR12}$	punch depth	1.52	1.58	mm
Material				
$z^{(6)} = \text{VAR22}$	sheet yield stress premultiplier	0.9	1.1	-
$z^{(7)} = \text{VAR23}$	c_1 strain rate dependent model	1	3	-
$z^{(8)} = \text{VAR24}$	c_2 strain rate dependent model	0.3	0.7	-
$z^{(9)} = \text{VAR27}$	spring stiffness punch	1000	26000	N/mm
$z^{(10)} = \text{VAR29}$	friction coefficient	0	0.2	-

5 Approximating the Finite Element Analyses

It takes approximately 15 minutes for the FE-model to generate a solution. As production speeds range between 12 to 60 rpm the FE-model is too slow for use in a control algorithm. In this chapter a fast and accurate substitute for the FE analysis is sought. The objective is to reduce the result space using a Proper Orthogonal Decomposition (section 5.1). Thereafter a meta model based on the input parameters is fitted through the reduced result space using Radial Basis Functions (section 5.2).

5.1 Proper Orthogonal Decomposition

Proper Orthogonal Decomposition (POD) is a method which enables to build a low dimensional approximation of a high dimensional problem. In this section POD is used to approximate the results of a finite element analysis.

Each point in the parameter space from the initial DOE (\mathbf{z}_m) defined in section 4.3 is used as input for a finite element analysis. In total 4960 simulations were done. Seven simulations failed, therefore 4953 complete force curves were generated.

The FE analyses were done using a variable time step. The average amount of steps needed was 290, whereas the minimum was 228 and the maximum was 552. To be able to compare the force curves each curve is interpolated in exactly $N = 200$ time steps ($F(t_n)$). Note that by interpolating with less time steps than in the original simulation the force curve is slightly smoothed. The force sensors in the production line as presented in section 2.2 do not measure negative forces. This can be seen clearly in the experimental force curve in Figure 1.2a. This is incorporated in the approximation by setting all negative forces equal to 0. These force curves are called *snapshots* in POD jargon [1]. The collection of M snapshots can be stored in a so-called snapshot matrix (\mathbf{F}). So, \mathbf{F} is an N by M matrix containing the $M = 4953$ force curves generated using the FE-model, in $N = 200$ time steps.

$$\mathbf{F} = [F_{nm}] = [F_m(t_n)] \quad \text{with } n = 1..N \\ m = 1..M \quad (5.1)$$

$$= \begin{bmatrix} F_1(t_1) & \cdots & F_M(t_1) \\ \vdots & \ddots & \vdots \\ F_1(t_N) & \cdots & F_M(t_N) \end{bmatrix}$$

To explain the principle of proper orthogonal decomposition an example with $N = 2$ results per snapshot and $M = 3$ snapshots is given. Consider 3 force curves at time step t_n and t_{n+1} . Normally these would be represented as in Figure 5.1a. However, the snapshot matrix can be considered as a set of M , N -dimensional vectors as well [1]. These three vectors are normalized and plotted in Figure 5.1b.

Instead of looking at the force curves in the current basis, a new basis is sought as such that the projection of all force curves is maximum. This new basis is called the POD basis (Φ) and is, depending on the dimensions of the snapshot matrix, an $N \times M$ or $N \times N$ matrix. In this work $N < M$ and the POD directions are just the eigenvectors (\mathbf{v}_j) of the matrix $\mathbf{C} = \mathbf{F} \cdot \mathbf{F}^T$ [2].

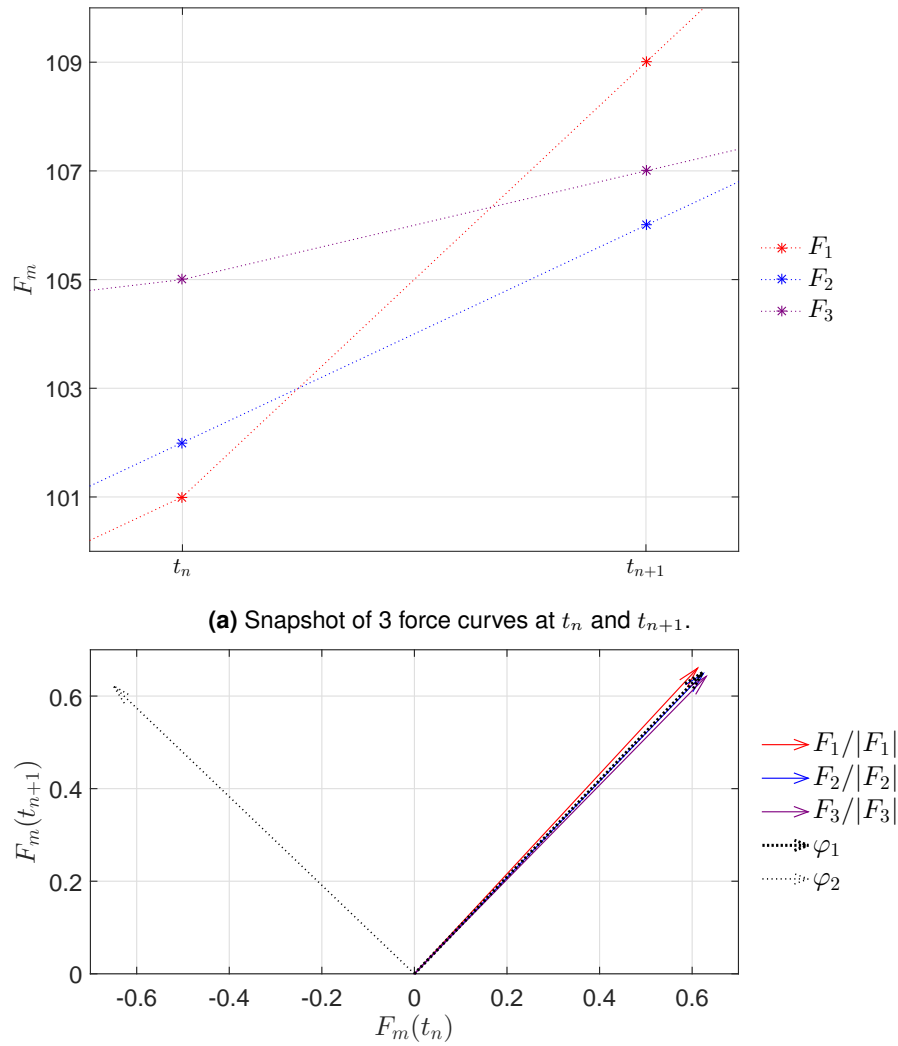
$$\varphi_j = \mathbf{v}_j \quad \text{with } j = 1..N \quad (5.2)$$

The total POD basis can be built by storing the POD directions in descending order of corresponding eigenvalues [1]. The POD directions have size $N \times 1$. Hence, by storing the N POD directions the total POD basis has size $N \times N$.

$$\Phi = [\varphi_1 \cdots \varphi_j \cdots \varphi_N] \quad (5.3)$$

All force curves in the snapshot matrix can be obtained by multiplying the POD basis with a so-called amplitude matrix \mathbf{A} .

$$\mathbf{F} = \Phi \cdot \mathbf{A} \quad (5.4)$$



(b) Force curves represented as $M = 3$, $N = 2$ -dimensional vectors with corresponding POD basis.

Figure 5.1: Two different representations of a force curve.

As the POD basis is orthogonal it holds that $\Phi^T \cdot \Phi = \mathbf{I}$ and the amplitude matrix can be calculated easily.

$$\mathbf{A} = \Phi^T \cdot \mathbf{F} \quad (5.5)$$

Force curve in the POD basis

A single force curve \mathbf{F}_m can be obtained by multiplying the POD basis with a corresponding amplitude vector \mathbf{a}_m . This amplitude vector is the m -th column of the amplitude matrix and contains all amplitudes corresponding to the j -th POD direction of force curve \mathbf{F}_m . Note that this can also be written as the multiplication of a POD direction (φ_j) with its corresponding amplitude scalar (A_{jm}) and summing over the number of POD directions (N).

$$\begin{aligned} \mathbf{F}_m &= \Phi \cdot \mathbf{a}_m \\ &= \sum_{j=1}^N \varphi_j \cdot A_{jm} \end{aligned} \quad (5.6)$$

Coming back to the example with the three force curves at times t_n and t_{n+1} . The first POD direction (φ_1) is plotted in Figure 5.1b. One can see that the first POD direction is very similar to the three

vectors representing the force curve. So, apparently not all POD directions are needed to represent the force curves. By using the first POD direction only, one can already get a good representation of a force curve. Hence, the force curves in the snapshot matrix can be approximated in a lower dimension by truncating the POD basis and amplitude matrix. The number of POD directions in the truncated POD basis (N_φ) is not established.

$$\mathbf{F} \approx \bar{\Phi} \cdot \bar{\mathbf{A}} \quad (5.7)$$

where,

$$\begin{aligned} \bar{\Phi} = [\Phi_{nj}], \bar{\mathbf{A}} = [A_{jm}] & \quad \text{with } j = 1..N_\varphi < N \\ & \quad m = 1..M \\ & \quad n = 1..N \end{aligned}$$

In the approximation of the FE model the principle is the same, only $N = 200$ and $M = 4953$. The number of POD directions needed in the truncated POD basis (N_φ) to capture the behavior as seen in Figure 4.3 is not known yet. In Figure 5.2 the first four normalized POD directions are plotted. One can see that the first POD direction looks very much like the force curve in Figure 3.5.

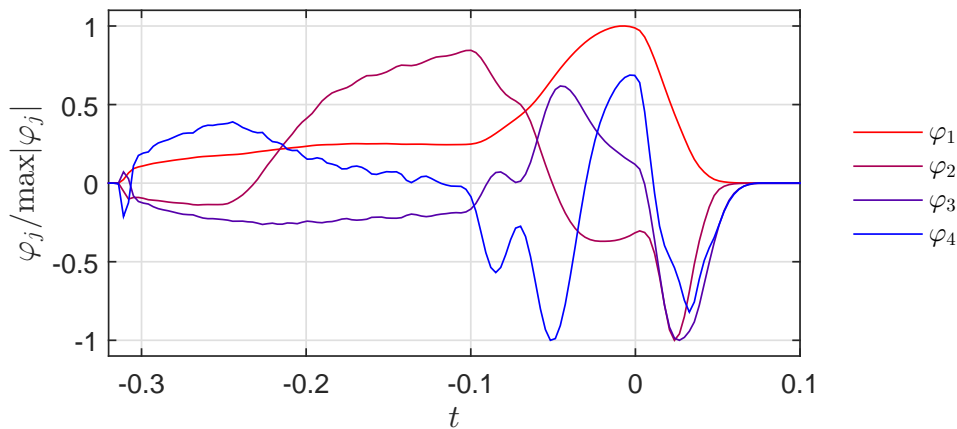


Figure 5.2: First 4 POD directions.

To find out how many POD directions are needed to represent the force curve the Root Mean Square Error (RMSE) is introduced. The RMSE is a measure for the difference between the force curve from the finite element analysis and the force curve in the truncated POD basis. The difference between the two force curves is squared and averaged over the number of time steps (N). Subsequently the square root is taken. Note that an interpolated force curves from the FE model can be written directly in the POD basis by combining equation 5.4 and 5.4.

$$\mathbf{F}_{\text{POD}} = \bar{\Phi} \cdot \bar{\Phi}^T \cdot \mathbf{F} \quad (5.8)$$

And the RMSE can be defined as:

$$\text{RMSE}(\mathbf{z}_m, N_\varphi) = \sqrt{\frac{1}{N} \sum_{n=1}^N \left(F_{\text{FEM}}(t_n, \mathbf{z}_m) - F_{\text{POD}}(t_n, \mathbf{z}_m, N_\varphi) \right)^2} \quad (5.9)$$

where

$$\begin{aligned} F_{\text{FEM}}(t_n, \mathbf{z}_m) &= \mathbf{F}_m \\ F_{\text{POD}}(t_n, \mathbf{z}_m, N_\varphi) &= \bar{\Phi} \cdot \bar{\Phi}^T \cdot \mathbf{F}_m \end{aligned}$$

Note that every force curve can thus be split in a part within the POD basis and a part outside the POD basis. Recall that in this work $N < M$ and the original POD basis had size $N \times N$.

$$F(t_n) = \left(\sum_{j=1}^{N_\varphi} \Phi_{nj} \cdot \Phi_{nj}^T \right) \cdot F(t_n) + \left(\sum_{j=N_\varphi+1}^N \Phi_{nj} \cdot \Phi_{nj}^T \right) \cdot F(t_n) \quad (5.10)$$

The error due to truncation of the POD basis can thus be defined as:

$$\bar{e}(t_n) = \left(\sum_{j=N_\varphi+1}^N \Phi_{nj} \cdot \Phi_{nj}^T \right) \cdot F(t_n) \quad (5.11)$$

Which is the same as $F_{\text{FEM}}(t_n) - F_{\text{POD}}(t_n, N_\varphi)$, the error in equation 5.9. For every point in the parameter space \mathbf{z}_m the root mean square error is calculated using a different number of POD-directions. The average root mean square error ($\overline{\text{RMSE}}$) over all force curves M is calculated and plotted in Figure 5.3.

$$\overline{\text{RMSE}}(N_\varphi) = \frac{1}{M} \sum_{m=1}^M \text{RMSE}(\mathbf{z}_m, N_\varphi)$$

Theoretically the average root mean square error due to truncation should be 0 when $N_\varphi = N$. At $N_\varphi \approx 170$ the average root mean square error drops to the computational error and could therefore not be calculated.

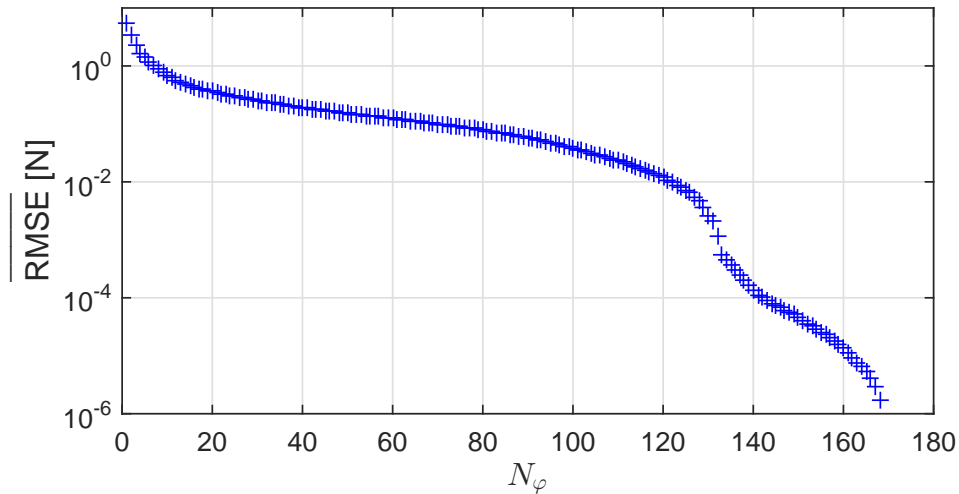


Figure 5.3: Average root mean squared error of the POD basis based on the initial DOE (\mathbf{z}_m) versus the number of used POD directions (N_φ).

5.2 Radial Basis Function

With the truncated amplitude matrix the force curves can only be obtained for the set of input parameters (\mathbf{z}_m). So, now the goal is to approximate the force curve for any set of parameters \mathbf{z} , instead of one of the sets of input parameters.

$$\hat{\mathbf{F}}(\mathbf{z}) = \bar{\Phi} \cdot \hat{\mathbf{a}}(\mathbf{z}) \quad (5.12)$$

Hence, a function should be found to predict the amplitude vector for any set of parameters $\hat{\mathbf{a}}(\mathbf{z})$. This is done by interpolating the set of known amplitudes for each POD direction throughout the parameter space. Hence, each row of the amplitude matrix (\mathbf{a}_j) is interpolated in \mathbf{Z}^D . To do this, Radial Basis Functions (RBF) are chosen as an interpolation method.

It is assumed that the amplitude scalar $\hat{A}_j(\mathbf{z})$ for every j -th POD direction can be written as the linear combination of a weight (w_k) and a radial basis function (ψ) [4]. This RBF is some function based of the euclidean distance between the argument (\mathbf{z}) and the known points in the parameter space (\mathbf{z}_k).

$$\hat{A}_j(\mathbf{z}) = \sum_{k=1}^M w_k \cdot \psi(\mathbf{z}_k - \mathbf{z}) \quad (5.13)$$

By evaluating the amplitude scalar $\hat{A}_j(\mathbf{z})$ on the known points in the parameter space (\mathbf{z}_m) the unknown weights can be found.

$$A_{jm} = \hat{A}_j(\mathbf{z}_m) \quad (5.14)$$

Doing this for all points in the parameter space gives:

$$\begin{aligned} \mathbf{a}_j &= \sum_{k=1}^M w_k \cdot \psi(\mathbf{z}_k - \mathbf{z}_m) \\ &= \sum_{k=1}^M w_k \cdot \Psi_{km} = \mathbf{w} \cdot \Psi \end{aligned} \quad (5.15)$$

Leading to:

$$\mathbf{w} = \mathbf{a}_j \cdot \Psi^{-1} \quad (5.16)$$

Where \mathbf{w} is the $1 \times M$ vector containing the weights for all M basis functions and Ψ is the matrix containing the radial basis functions evaluated at all M points. Substituting equation 5.16 into equation 5.13 gives an expression for the amplitude scalar for the j -th POD direction for any set of input parameters:

$$\hat{A}_j(\mathbf{z}) = \mathbf{a}_j \cdot \Psi^{-1} \cdot \psi(\mathbf{z}_k - \mathbf{z}) \quad (5.17)$$

Now the function to predict the amplitude vector $\hat{\mathbf{a}}(\mathbf{z})$ can be defined as the vector collecting the N_φ approximated amplitude scalars.

$$\hat{\mathbf{a}}(\mathbf{z}) = \hat{A}_j(\mathbf{z}) \quad \text{with } j = 1..N_\varphi \quad (5.18)$$

The above-mentioned generally holds for all types of radial basis functions. In this work the choice is made to use a multiquadric radial basis function with scaling in each dimension.

$$\psi(\mathbf{z}_k - \mathbf{z}) = \sqrt{c_k^2 + \|\boldsymbol{\theta} \circ (\mathbf{z}_k - \mathbf{z})\|^2} \quad (5.19)$$

herein c_k is a local shape parameter and $\boldsymbol{\theta}$ a global scaling parameter [4]. The global scaling parameter $\boldsymbol{\theta}$ scales the parameter space in each dimension as follows.

$$\|\boldsymbol{\theta} \circ (\mathbf{z}_k - \mathbf{z})\| = \sqrt{\sum_{d=1}^D \theta_d \left(z_k^{(d)} - z^{(d)} \right)^2} \quad (5.20)$$

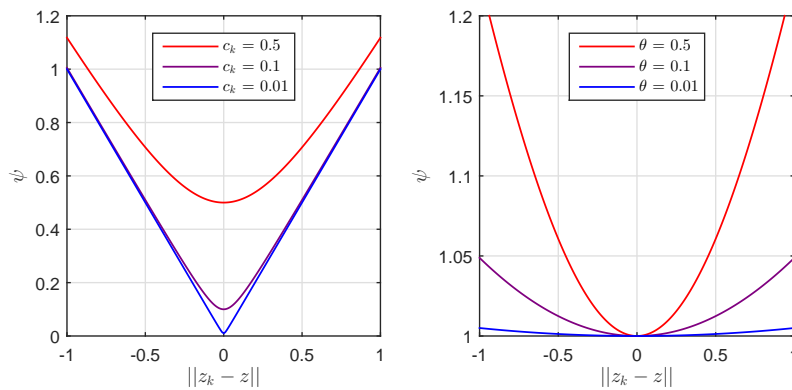
The values for θ can either be fixed or optimized per dimension. When θ is chosen to be same in each dimension a value of $\theta_d = \sqrt[d]{M}$ is suitable when using a normalized \mathbf{z} . The optimization of θ is done by means of a Leave One Out Cross-Validation (LOOCV). The cross-validation values ϵ_m can be found easily. By minimizing the euclidean norm of ϵ_m the optimal values for θ can be found [4].

$$\epsilon_m = \hat{A}_j^{(-m)}(\mathbf{z}_m) - A_{jm} = \frac{w_k}{(\Psi^{-1})_{kk}} \quad (5.21)$$

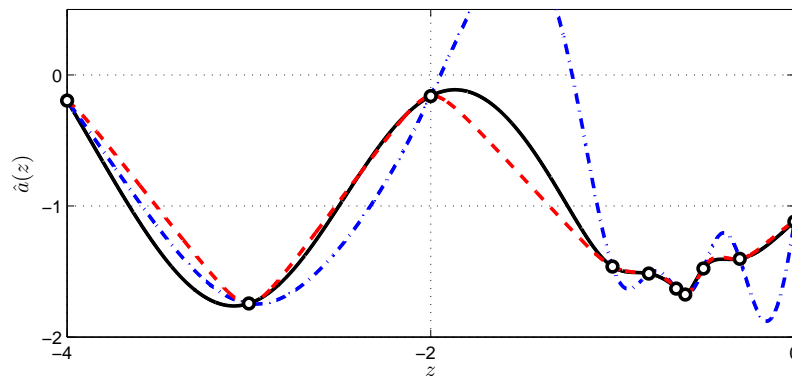
The local shape parameters c_k can be fixed or scaled to their nearest neighbor. When c_k is scaled to its nearest neighbor the values for c_k can be calculated as follows [4].

$$c_k = \frac{\min_{k \neq m} \|\theta \circ (\mathbf{z}_k - \mathbf{z}_m)\|}{\max_m c_m} \quad (5.22)$$

The influence of changing both parameters in the multiquadric radial basis function can be found in Figure 5.4. As one can see in Figure 5.4a changing c_k and θ has the opposite effect. Lowering c_k gives a steeper radial basis function, whereas increasing θ gives a steeper function. In Figure 5.4b the result of changing c_k and θ in an interpolation can be found. The red line is an interpolation with c_k constant, and high θ . This leads to a steep function in the area with few data points ($z = -4..-1$). The blue line is an interpolation with c_k constant, and low θ . This gives large oscillations in area with many data points ($z = -1..0$). In black the interpolation function with c_k scaled to its nearest neighbor is plotted. One can see that this interpolation fits the data points nicely in both the area with few data points as the area with many data points.



(a) Multiquadric radial basis function (ψ). On the left: varying the shape parameter (c_k) and fixed scaling ($\theta = 1$). On the right: fixed shape parameter ($c_k = 1$) and varied scaling (θ).



(b) Interpolation using a radial basis function with: c_k fixed and high θ (red), c_k fixed and low θ (blue) and c_k scaled to the nearest neighbor (black).

Figure 5.4: Influence of different parameters in a multiquadric radial basis function.

5.3 Force curves using a PODRBF approximation

Now a force curve based on any point in the parameter space \mathbf{z} can be approximated using PODRBF as follows.

$$\begin{aligned} F_{\text{PODRBF}}(t_n, \mathbf{z}, N_\varphi) &= \bar{\Phi} \cdot \hat{\mathbf{a}}(\mathbf{z}) \\ &= \sum_{j=1}^{N_\varphi} \varphi_j \cdot \hat{A}_j(\mathbf{z}) \end{aligned} \quad (5.23)$$

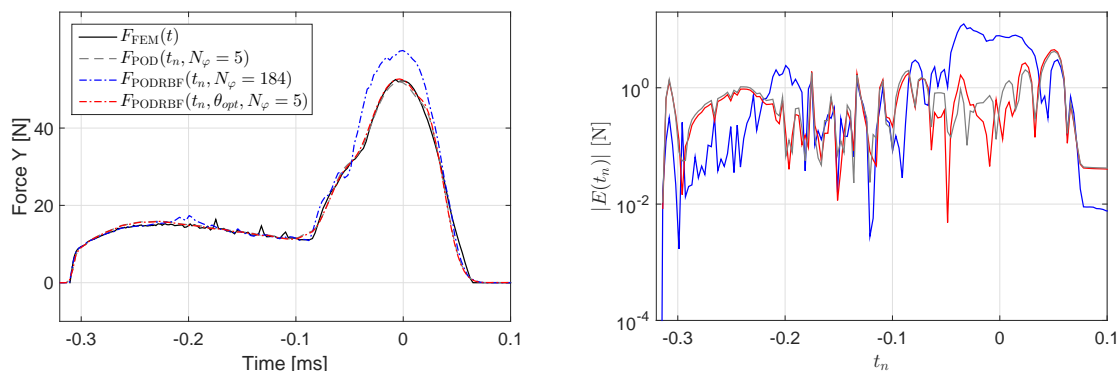
The radial basis functions are scaled to their nearest neighbor (c_k) and fitted using a fixed scaling of $\theta = \sqrt[10]{5000} \approx 2.3$ for the first 184 POD directions and an optimized scaling for the first 25 POD directions. To test the quality of both PODRBF-models extra points in the parameter space are generated. This is done by calculating the minimum Euclidean distance between a new LHS of 1000 points and the original DOE. The 100 points p with maximum Euclidean distance with respect to the original DOE are chosen as a validation set.

So, to recapitulate there are 5 types of force curves:

- $F_{\text{FEM}}(t)$, a force curve from the FE-model.
- $F_{\text{FEM}}(t_n)$, a force curve from the FE-model discretized in N time steps.
- $F_{\text{POD}}(t_n, N_\varphi)$, a force curve from the FE-model projected in the truncated POD basis.
- $F_{\text{PODRBF}}(t_n, N_\varphi)$, a force curve approximated using radial basis functions with fixed scaling.
- $F_{\text{PODRBF}}(t_n, N_\varphi, \theta_{\text{opt}})$, a force curve approximated using radial basis function with optimized scaling.

The force curves from the FE-model are based on points in the parameter space from either the original DOE (\mathbf{z}_m) or the validation set (\mathbf{z}_p , with $p = 1..100$). The PODRBF approximation is defined throughout the whole parameter space (\mathbf{Z}^D) and can therefore be based on any point (\mathbf{z}).

In Figure 5.5a different types of force curves based on a point from the validation set are plotted (\mathbf{z}_p). One can see that the force curve plotted directly from the FE-model shows peaks in the free bending stage. This high frequent behavior is due to numerical noise. The force curve from the FE-model is projected in a truncated POD basis with $N_\varphi = 5$. With this few POD directions the sudden change in slope initiated by the change in contact area (see Figure 3.5) is captured poorly. The PODRBF approximation with fixed scaling and $N_\varphi = 184$ overestimates the force curve, specially around the maximum force. However, the approximation does capture the sudden change in slope. An approximation with this many POD directions starts to show high frequent behavior. The PODRBF approximation with optimized scaling and $N_\varphi = 5$ is almost identical to the original force curve written in the POD basis.



(a) Force curve from the FE-model, written in the POD basis and using a PODRBF approximation with fixed scaling and optimized scaling.

(b) Absolute error per time step of the interpolated force curve from the FE-model compared to the POD basis, the PODRBF approximation with fixed and optimized scaling.

Figure 5.5: Different approximations of the force curve and their absolute error per time step.

Table 5.1: Amplitudes corresponding to the first 5 POD directions of the force curves in Figure 5.5a.

	φ_1	φ_2	φ_3	φ_4	φ_5
A_{POD}	267.43	-25.97	-64.76	-6.71	16.47
A_{PODRBF}	303.17	-40.04	-63.59	-5.25	3.18
$A_{\text{PODRBF}}(\theta_{\text{opt}})$	269.90	-27.98	-64.19	-5.57	14.18

In Figure 5.5b the absolute error between the interpolated curve from the FE-model and the different approximations is plotted.

$$|E(t_n)| = \left| F_{\text{FEM}}(t_n, \mathbf{z}_p) - F_{\text{approx}}(t_n, \mathbf{z}_p) \right| \quad (5.24)$$

The curve of the absolute error of the PODRBF approximation using optimized scaling (in red) is very similar to the absolute error of the force curve written in the POD basis with $N_\varphi = 5$ (in gray). Only around $t = 0$ the absolute errors differ slightly. The absolute error of the PODRBF approximation with fixed scaling looks completely different from the two other curves (in blue).

In Table 5.1 the amplitudes corresponding to the first 5 POD directions are given. As expected from Figure 5.5 the amplitudes of the force curve projected in the POD basis and the PODRBF approximation with optimized scaling are alike. The PODRBF approximation with fixed scaling show large deviations from the correct amplitudes.

The average root mean square error between F_{FEM} and F_{PODRBF} over the total validation set is calculated (see equation 5.9) and plotted in Figure 5.6.

$$\overline{\text{RMSE}}(N_\varphi) = \frac{1}{P} \sum_{p=1}^P \text{RMSE}(\mathbf{z}_p, N_\varphi) \quad (5.25)$$

However, the RMSE between the force curve from the FE-model projected in the POD basis with N_φ POD-directions (F_{POD}) and the PODRBF approximation (F_{PODRBF}) can be calculated as well.

$$\text{RMSE}(\mathbf{z}_p, N_\varphi) = \sqrt{\frac{1}{N} \sum_{n=1}^N \left(F_{\text{POD}}(t_n, \mathbf{z}_p, N_\varphi) - F_{\text{PODRBF}}(t_n, \mathbf{z}_p, N_\varphi) \right)^2} \quad (5.26)$$

where

$$\begin{aligned} F_{\text{POD}}(t_n, \mathbf{z}_p, N_\varphi) &= \bar{\Phi} \cdot \bar{\Phi}^T \cdot \mathbf{F}_p \\ F_{\text{PODRBF}}(t_n, \mathbf{z}_p, N_\varphi) &= \bar{\Phi} \cdot \hat{\mathbf{a}}(\mathbf{z}_p) \end{aligned}$$

Leading to:

$$\text{RMSE}(\mathbf{z}_p, N_\varphi) = \sqrt{\frac{1}{N} \sum_{n=1}^N \left(\bar{\Phi} \cdot \left(\bar{\Phi}^T \cdot \mathbf{F}_p - \hat{\mathbf{a}}(\mathbf{z}_p) \right) \right)^2} \quad (5.27)$$

The latter RMSE gives an indication of how well the RBF predicts the amplitudes and thus the force curve. Both RMSE's are plotted in Figure 5.6. As one can see the RMSE between F_{FEM} and F_{PODRBF} using fixed scaling (in blue) does not become smaller than 2 N. By increasing the number of used POD directions to 20, the error between F_{FEM} and F_{PODRBF} is the same as the error between F_{POD} and F_{PODRBF} . So, adding an extra POD direction does not add any accuracy to the approximation.

By using a radial basis function with optimized scaling (in red) the RMSE between F_{FEM} and F_{PODRBF} can be lowered to 0.9 N by including 25 POD directions. Note that there is still a difference of 0.1 N between the two types of RMSE. Hence, adding extra POD directions would increase the accuracy of the approximation. However, due to the large computational costs it takes to fit an extra approximated amplitude scalar the choice was made to take this error of 0.9 N for granted. To give an interpretation of the size of this error, the average maximum force is 91.5 N which can thus be predicted with an error of 1%.

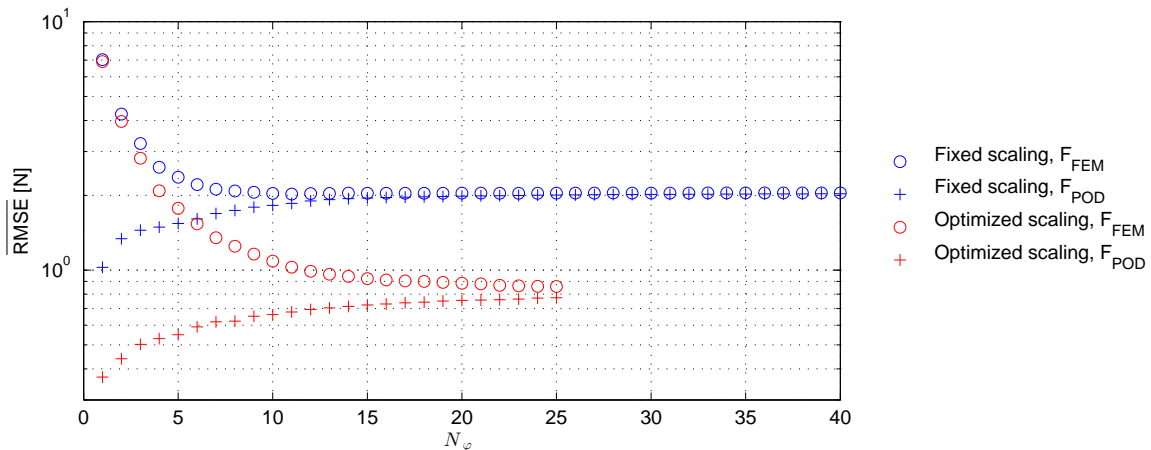


Figure 5.6: Average root mean squared error of the test set \mathbf{z}_p versus the number of used POD directions (N_φ) with fixed scaling of $\sqrt[10]{5000}$ and optimized scaling for the first 25 POD directions. RMSE between F_{FEM} and F_{PODRBF} is plotted with a circle, RMSE between F_{POD} with N_φ POD-directions and F_{PODRBF} is plotted with a + sign.

5.4 Variation 1-by-1 using a PODRBF approximation

Now all parameters are varied 1-by-1 in the PODRBF approximation with optimized scaling and $N_\varphi = 25$ to reproduce Figure 4.3. Note that in the remainder of this work those settings are used to approximate a force curve. So,

$$F_{\text{PODRBF}}(t_n, \mathbf{z}) = F_{\text{PODRBF}}(t_n, N_\varphi = 25\theta_{\text{opt}})$$

is evaluated using nominal settings (\mathbf{z}') and varying one parameter ($z^{(d)}$) at a time. Note that these points (\mathbf{z}) are not used to make the POD basis. For comparison the force curves from the FE-model at minimum and maximum values are plotted as well.

When comparing all plots in Figure 5.7 it can be seen that generally the force curves from the PODRBF-model are smoother than the curves from the FE-model. Abrupt changes in slope are not captured by the PODRBF-model. For example the slope of the curve upon initial contact is in most cases not as steep as in the FE-results. However, generally the characteristics in force curve each parameter causes are captured adequately.

Clearance die/fixed die

In Figure 5.7a one can see that the influence of the clearance is slightly overestimated by the PODRBF-model, the force curves lay above the curves of the FE-model.

X-alignment lower part

The alignment in x -direction of the lower part has a large influence on the timing of the force curve. The PODRBF approximation captures this behavior reasonably good as can be seen in Figure 5.7b. Remember that the POD basis was built without any negative forces (section 5.1). Strikingly the force curves from the PODRBF-model do drop to negative values.

Sheet thickness

In Figure 5.7c one can see that the influence of the sheet thickness is slightly underestimated by the PODRBF model. The shift in initial contact between punch and flap (t_0) is captured only after the initial contact took place.

Y-alignment die

In Figure 5.7d the force curves with varying y -alignment of the die are plotted. Except for the general remarks on the PODRBF approximation, the influence of the y -alignment of the die is accurately captured.

Punch depth

Upon initial contact the PODRBF approximation falls below zero for small punch depths as can be seen in Figure 5.7e. However all shifts in timing are precisely captured by the approximation.

Sheet yield stress premultiplier

In Figure 5.7f the force curves with varying sheet yield stress premultiplier are plotted. The peak in the force curve is somewhat more flat for a yield stress multiplier smaller than 1.

C1 strain rate dependent model

The influence of the material constant c_1 from the strain rate dependent model is captured pretty good as can be seen in Figure 5.7g. Around the maximum force the influence of c_1 is slightly underestimated.

C2 strain rate dependent model

As for c_1 , the influence of c_2 is underestimated around the maximum force as well. The force curves with varying c_2 can be found in Figure 5.7h.

Spring stiffness punch

In Figure 5.7i the force curves with varying spring stiffness of the punch are plotted. The influence of a low spring stiffness is overestimated, whereas the influence of a high spring stiffness is underestimated. The force curve from the PODRBF-model for $\gamma = 1000$ is, in contrast to all other curves, less smooth than the curve from the FE-model.

Friction coefficient

Figure 5.7j displays the force curves from various friction coefficients. Compared to Figure 4.3j the influence of varying the friction coefficient seems to be increased. However, note that in the PODRBF-model all friction coefficients are changed at once.

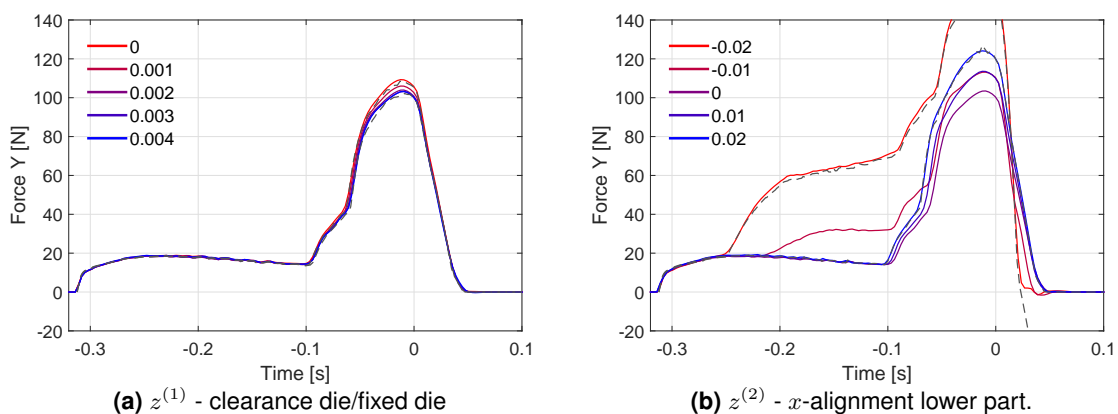


Figure 5.7: Force curves from a POD-RBF approximation for most influential parameters. Minimum and maximum force curves from FEA are plotted using gray dashed lines.

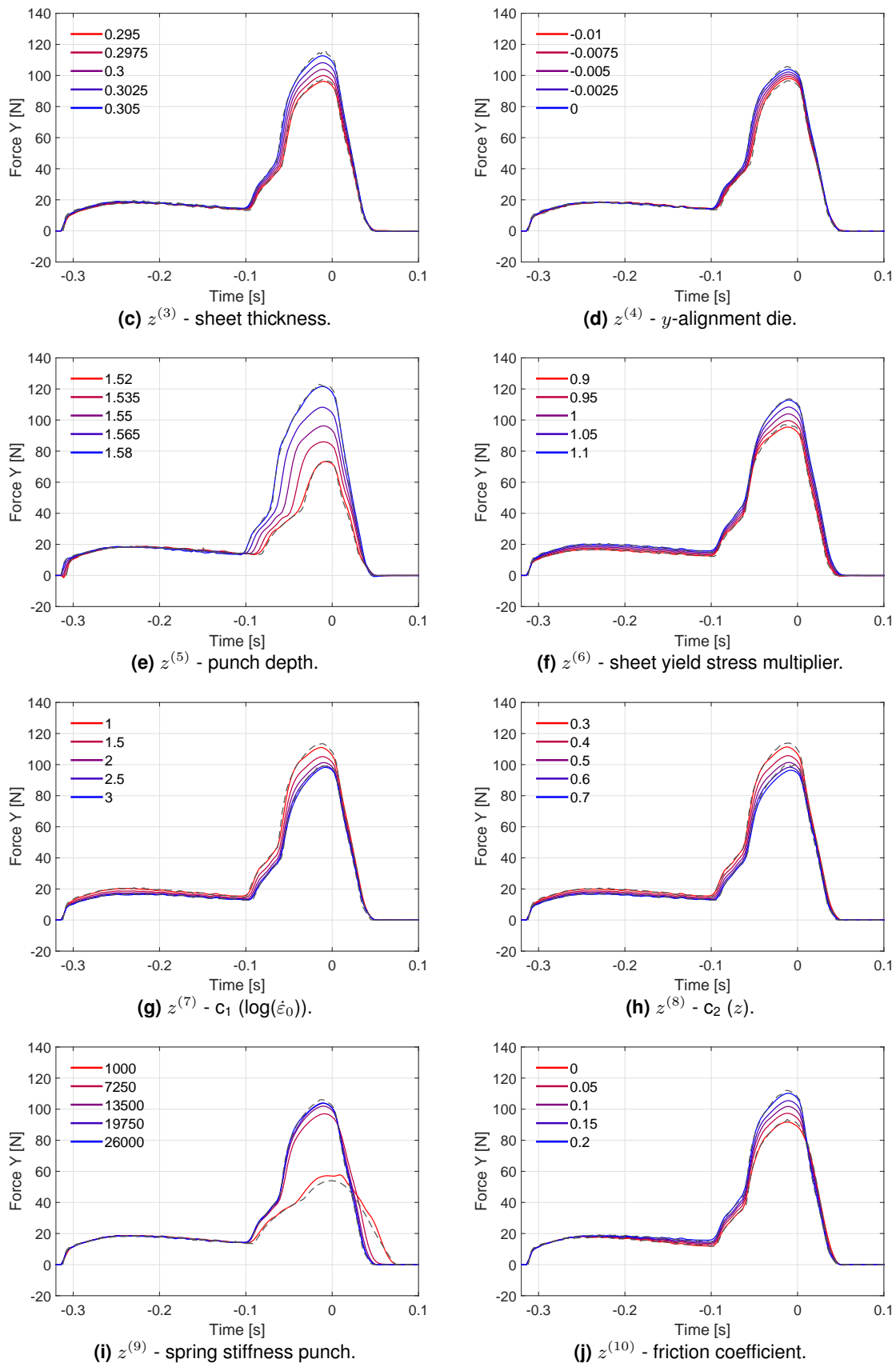


Figure 5.7: Force curves from a POD-RBF approximation for most influential parameters. Minimum and maximum force curves from FEA are plotted using gray dashed lines (cont.).

6 Inverse analysis

The goal of an inverse analysis is to estimate what input parameters could have caused a certain output. To be acquainted with the input parameters can be of great value in a control algorithm. For example, if a change in friction coefficient can be identified, tool wear can be detected. In this section the PODRBF-model is used to identify the input parameters of an experimental force curve. An experimental force curve $F_{\text{exp}}(t)$ can be:

- $F_{\text{FEM}}(t)$, a force curve based on the validation set \mathbf{z}_p which is not included in the original DOE (\mathbf{z}_m) on which the POD basis is build.
- $F_{\text{test}}(t)$, a force curve as measured in the test setup (see section 1.2).

To take into account the difference between the FE-model and the curves from the test setup the implementation of weight function is proposed in section 6.1.

Looking at Figure 5.3 with $N_\varphi = 25$ the force curves projected in the truncated POD basis have an RMSE due to truncation of 0.3 N. To see if the projection to the POD basis has an influence on the estimation of the input parameters two types of error functions are proposed in section 6.2. Lastly, based on the proposed weight and error functions a parameter estimation is done in section 6.3.

6.1 Weight Function

The PODRBF-model is based on force curves from a two-dimensional FE-model. As the test data comes from a process in the real world, any differences can be taken into account by implementing a weight function. A three-dimensional FE-model is build to quantify the difference between a two-dimensional and a three-dimensional problem.

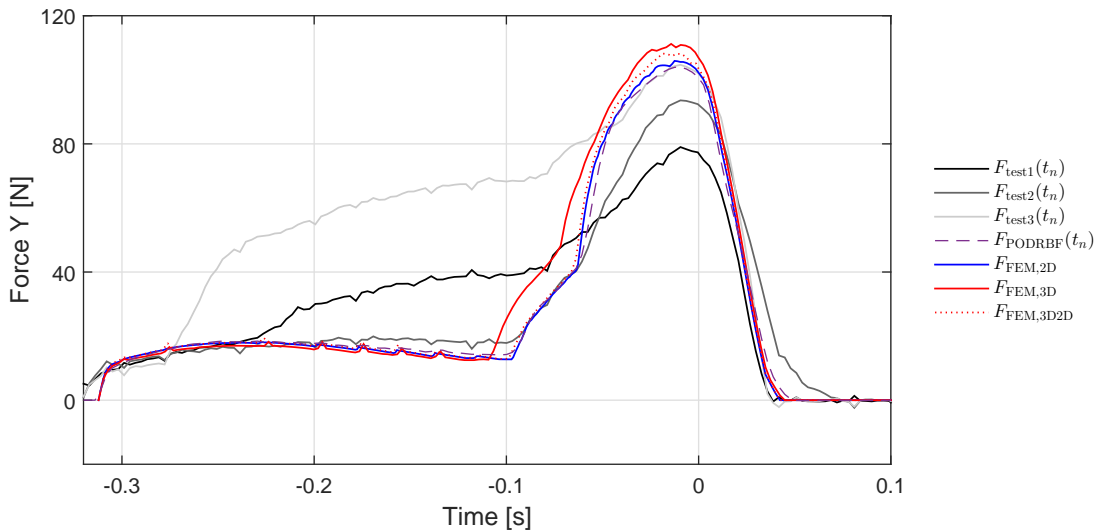


Figure 6.1: Force curves using nominal settings from the 2-dimensional model ($F_{\text{FEM},2\text{D}}$), a 3-dimensional model constrained to 2 dimensions ($F_{\text{FEM},3\text{D}2\text{D}}$), a 3-dimensional model ($F_{\text{FEM},3\text{D}}$) and the PODRBF approximation ($F_{\text{PODRBF}}(t_n)$). Three experimental force curves from one randomly chosen product as measured in the test setup ($F_{\text{test}}(t_n)$) are plotted for comparison.

The force curve from the three-dimensional FE-model ($F_{\text{FEM},3\text{D}}$), based on nominal settings, can be found in Figure 6.1. Compared to the curve from the two-dimensional model ($F_{\text{FEM},2\text{D}}$) one can see that the change in contact area is initiated earlier. This is due to the anticlastic bending of the flap.

A suitable weight function is 1 when the approximation is compatible with the real world, and close to 0 when the approximation differs from the real world. A weight function which fulfills these requirements is the following.

$$w(t_n) = 1 - \left| \frac{F_{\text{FEM},3\text{D}}(t_n, \mathbf{z}') - F_{\text{FEM},2\text{D}}(t_n, \mathbf{z}')}{\max(F_{\text{FEM},3\text{D}}(t_n, \mathbf{z}') - F_{\text{FEM},2\text{D}}(t_n, \mathbf{z}'))} \right| \quad (6.1)$$

Notice that there is a difference in initial contact between the test data and the FE-model in Figure 6.1. To compensate this, a ramp from $w(t_1 = -0.32) = 0.1$ to $w(t_8 = -0.3) = 1$ is added manually to the weight function. After $t = 0.1$ nothing of interest happens in the data from the test setup, therefore the weight function is ramped down to $w(t_N = 0.28) = 0.1$. To smooth the numerical noise of the FE analysis in the weight function a moving average filter with a span of 5 is used. The final weight function can be found in Figure 6.2.

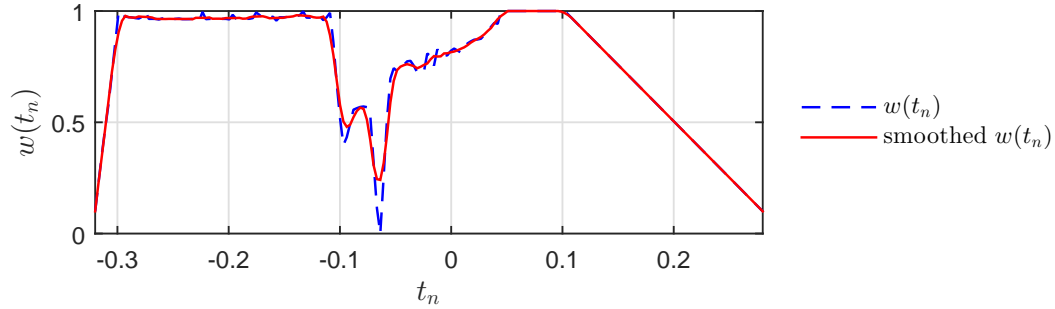


Figure 6.2: Weight function ($w(t_n)$) to compensate the difference between the two- and three-dimensional model. Original version is denoted with a blue dashed line, final smoothed version is denoted with a solid red line.

6.2 Error Function

The difference between an experimental force curve and a force curve from the PODRBF approximation, is a measure for how adequately a certain set of input parameters \mathbf{z} represent the experimental force. In this section different error functions based on this difference are proposed.

$$e(\mathbf{z}) = e(F_{\text{exp}} - F_{\text{PODRBF}}(\mathbf{z}))$$

The amplitude vector for any experimental force curve can be defined as the transposed truncated POD basis times the interpolated force curve.

$$\bar{\mathbf{a}}_{\text{exp}} = \sum_{n=1}^N \bar{\Phi}_{nj}^T \cdot F_{\text{exp}}(t_n) \quad (6.2)$$

Error function in time

When a force curve based on the validation set ($F_{\text{FEM}}(t_n, \mathbf{z}_p)$) is used as an experimental curve there is no need to incorporate a weight function. A suitable error function is the root mean square error (equation 5.9). Note that the error function consists of a constant part due to truncation.

$$\begin{aligned} e_t(\mathbf{z}) &= \text{RMSE}(\mathbf{z}) \\ &= \sqrt{\frac{1}{N} \sum_{n=1}^N (F_{\text{exp}}(t_n) - \bar{\Phi} \cdot \hat{\mathbf{a}}(\mathbf{z}))^2} \\ &= \sqrt{\frac{1}{N} \sum_{n=1}^N (\bar{\Phi} \cdot (\bar{\mathbf{a}}_{\text{exp}} - \hat{\mathbf{a}}(\mathbf{z})) + \bar{e}(t_n))^2} \end{aligned} \quad (6.3)$$

This error due to truncation is orthogonal to the truncated POD basis. Therefore it holds that:

$$\sum_{n=1}^N \bar{\Phi}_{nj}^T \cdot \bar{e}(t_n) = 0 \quad (6.4)$$

When the proposed weight function (Figure 6.2) must be incorporated, a time dependent error function is needed. The absolute difference between the two force curves is a suitable option.

$$e_t(t_n, \mathbf{z}) = |F_{\text{exp}}(t_n) - F_{\text{PODRBF}}(t_n, \mathbf{z})| \quad (6.5)$$

Now the weight can be incorporated by multiplying $e_t(t_n, \mathbf{z})$ with the weight function and taking the mean.

$$e_{t,w}(\mathbf{z}) = \text{mean}(w(t_n) \cdot e(t_n, \mathbf{z})) \quad (6.6)$$

Error function in POD basis

It is intuitive to define an error function in time. However, the error function can be defined directly in the POD basis as well. Without the incorporation of a weight function, the error function in the POD basis (e_A) is defined as the root mean square error between the experimental amplitude vector (equation 6.2) and the amplitude vector from the PODRBF approximation (equation 5.18).

$$e_A(\mathbf{z}) = \sqrt{\frac{1}{N_\varphi} \sum_{j=1}^{N_\varphi} (\bar{\mathbf{a}}_{\text{exp}} - \hat{\mathbf{a}}(\mathbf{z}))^2} \quad (6.7)$$

By neglecting the error outside the truncated POD basis, both error functions relate directly by:

$$e_t(\mathbf{z}) = e_A(\mathbf{z}) \sqrt{\frac{1}{N} \sum_{n=1}^N \sum_{j=1}^{N_\varphi} (\Phi \circ \Phi)_{nj}} \quad (6.8)$$

The relation between the error function in time and the error function in the POD basis is plotted in Figure 6.3. With $N_\varphi = 200$ the root in becomes 1, in that case $e_t(\mathbf{z}) = e_A(\mathbf{z})$. Therefore it follows directly that $e_t(\mathbf{z}) \leq e_A(\mathbf{z})$. With $N_\varphi = 25$ as used in this work, the error function in the POD basis (e_A) is approximately three times larger than the error function in time (e_t).

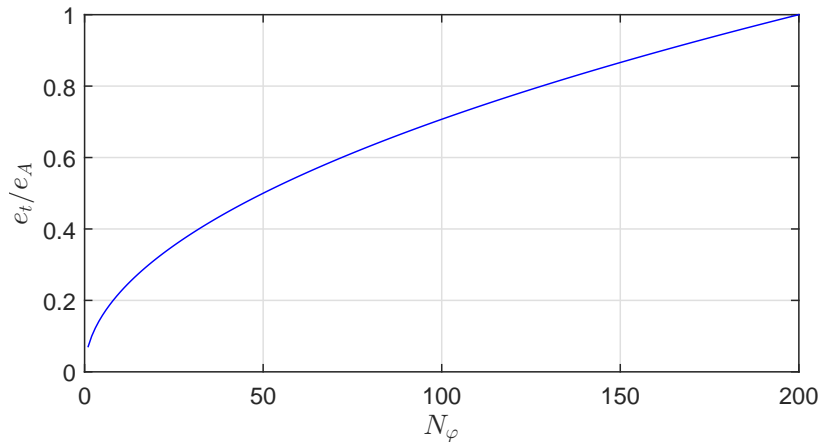


Figure 6.3: Relation between e_t and e_A as described in equation 6.8.

The time dependent weight function can be transformed to a function of j by premultiplying with the transpose of the truncated POD basis.

$$w(j) = \sum_{n=1}^N \bar{\Phi}_{nj}^T \cdot w(t_n) \quad (6.9)$$

The error function in the truncated POD basis is defined as the absolute difference between both amplitude vectors.

$$e_A(j, \mathbf{z}) = |\mathbf{a}_{\text{exp}} - \hat{\mathbf{a}}(\mathbf{z})| \quad (6.10)$$

Again, the weighted error function is defined as the mean of the weight function times the error function.

$$e_{A,w}(\mathbf{z}) = \text{mean}(w(j) \cdot e(j, \mathbf{z})) \quad (6.11)$$

6.3 Parameter estimation

The smallest evaluation of the error function is the most adequate representation of the set of input parameters \mathbf{z} . Hence, to do a parameter estimation the objective is to minimize the proposed error functions.

$$\min e(\mathbf{z}) \quad (6.12)$$

Estimating the validation set

By estimating the parameters of the known validation set (\mathbf{z}_p) the ability of the unweighted error functions to predict the correct parameters can be examined. In Figure 6.4 the error percentages of a series of parameter estimations based on time can be found. In Figure 6.5 the error percentages from a parameter estimation based on the amplitude can be found. The number of parameters to be identified is varied (D). The parameters which are estimated are chosen randomly during the inverse analysis. Hence, only when all the parameters are estimated ($D = 10$) the series of parameter estimations based on amplitude and time are the same. More on this series of parameter estimations can be found in Appendix C.

When only one parameter is estimated ($\mathbf{Z}^{(D=1)}$) the other 9 parameters ($\mathbf{z}_p^{(d-D)}$) are given to the error function. With only one parameter to be estimated, $D = 1$, the average error is 9% for both the error function based on time and on amplitude.

For both error functions the average error percentages increase to around 20% for an estimation of all ten parameters. Generally there is very little difference in average error between both error functions. The number of iterations and function evaluations needed is slightly lower for the error function defined in the POD basis. However, the differences are marginally.

When 10 parameters are estimated the full parameter space ($\mathbf{Z}^{(D=10)}$) has to be investigated. Parameters which are found with an average error less than 10% in the full parameter space are considered to be estimated accurately. As can be seen in Figure 6.4 and 6.5 this criteria holds for both error functions for the following three parameters:

- punch depth $z^{(5)}$
- spring stiffness punch $z^{(9)}$
- friction coefficient $z^{(10)}$

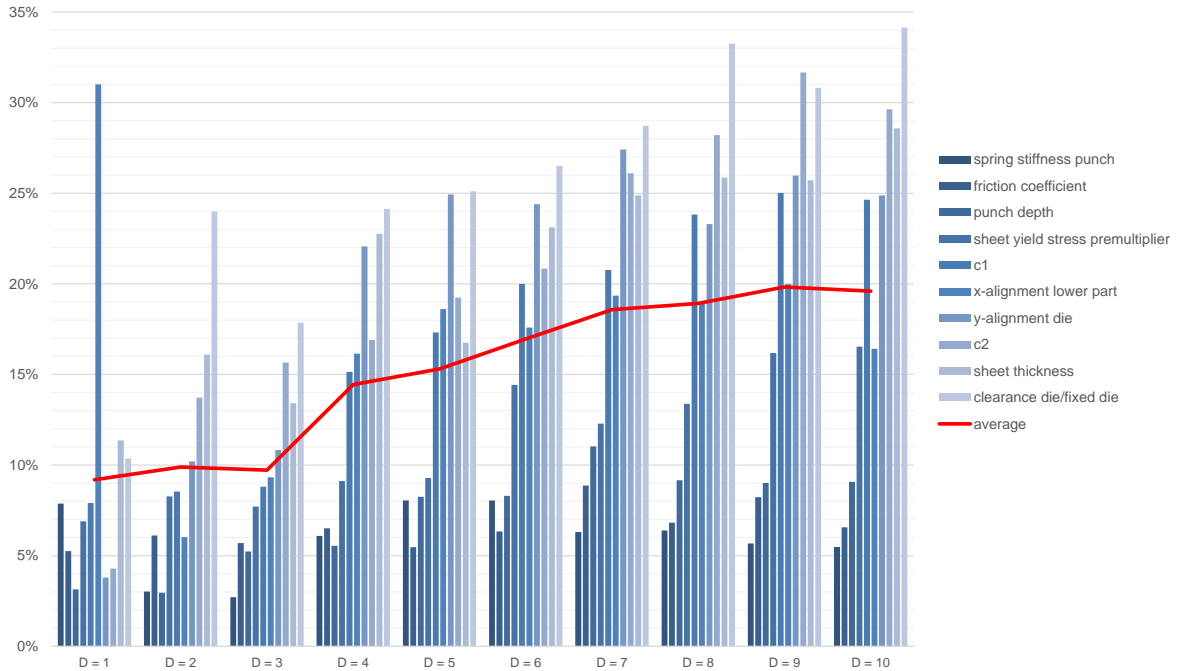


Figure 6.4: Error percentages of a parameter estimation on the validation set (\mathbf{z}_p) based on time (e_t) using different number of parameters to be estimated (D).

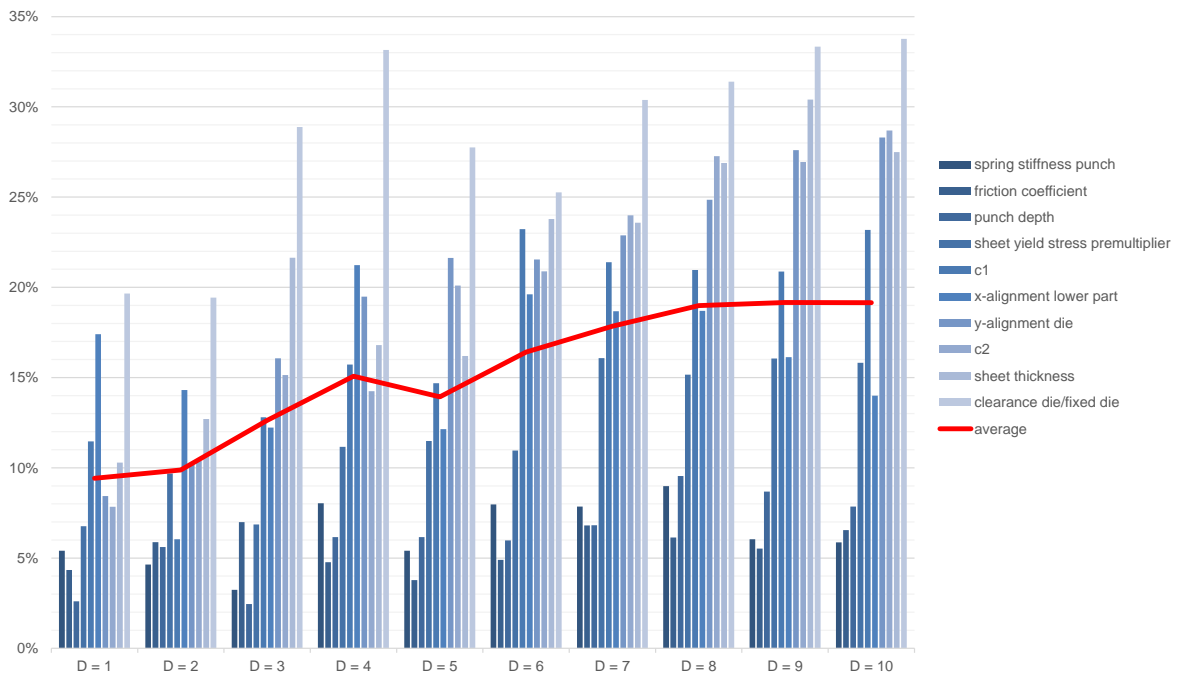


Figure 6.5: Error percentages of a parameter estimation on the validation set (\mathbf{z}_p) based on amplitude (e_A) using different number of parameters to be estimated (D).

Evaluation per parameter

The error function in all dimensions is checked for local minima. To do this a point from the validation set is chosen randomly. Each parameter is varied separately from minimum to maximum and the RMSE is evaluated based on both the amplitude and time. The results can be found in Figure 6.6.

As expected from the relation between the error function in time and in the POD basis (see equation 6.8) the RMSE defined in the POD basis is three times larger than the error in time.

The punch depth (Figure 6.6e), the spring stiffness of the punch (Figure 6.6i) and the friction coefficient (Figure 6.6j) which are estimated accurately in the estimation the validation set, show large variation in RMSE. The clearance between the die and fixed die (Figure 6.6a) and the x -alignment of the lower part (Figure 6.6b) show large variation as well. The x -alignment of the lower part shows a local minimum when $|z^{(2)}|$ approaches 1. This in agreement with the force curves varied 1-by-1 (Figure 4.3 and 5.7) where both the minimum and maximum with respect to the nominal value give rise to a larger maximum force.

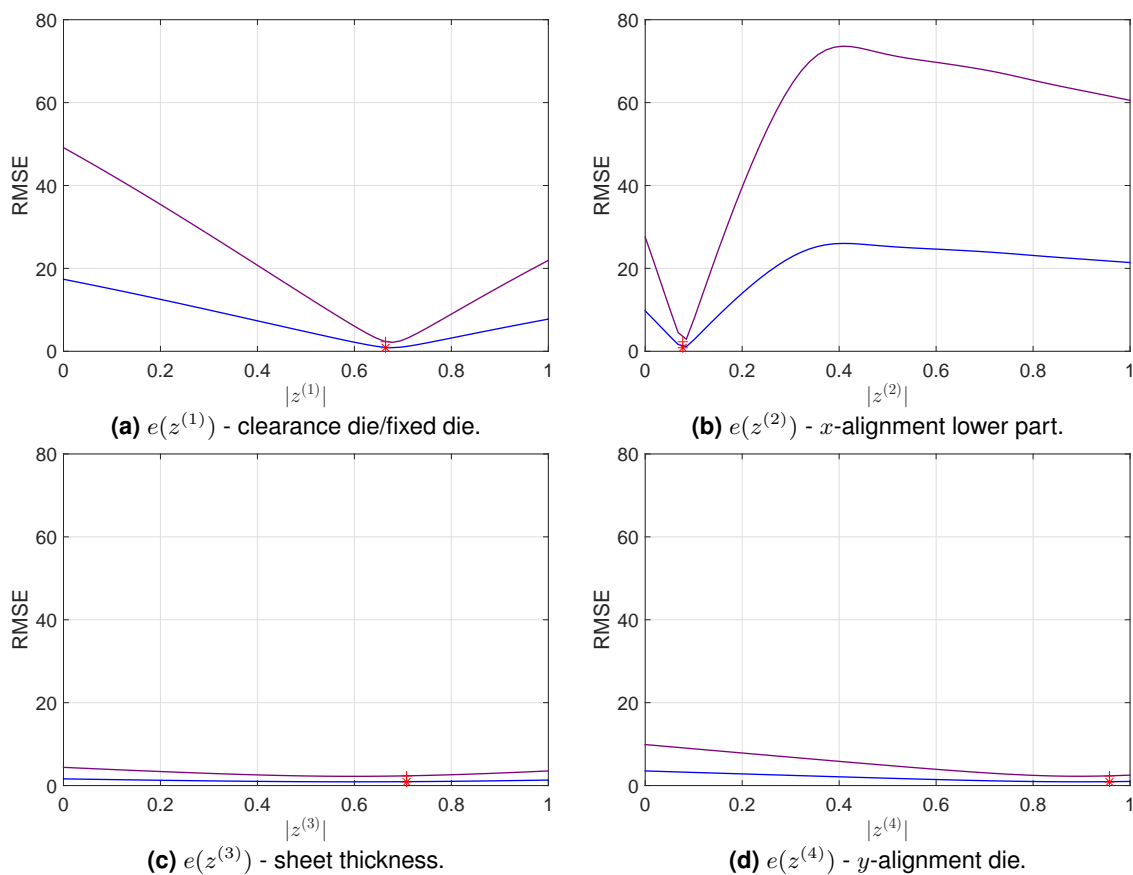


Figure 6.6: RMSE evaluated per dimension: e_t is denoted with a blue line, e_A denoted with a purple line. In red, both error function evaluated on \mathbf{z}_p with $p = 32$.

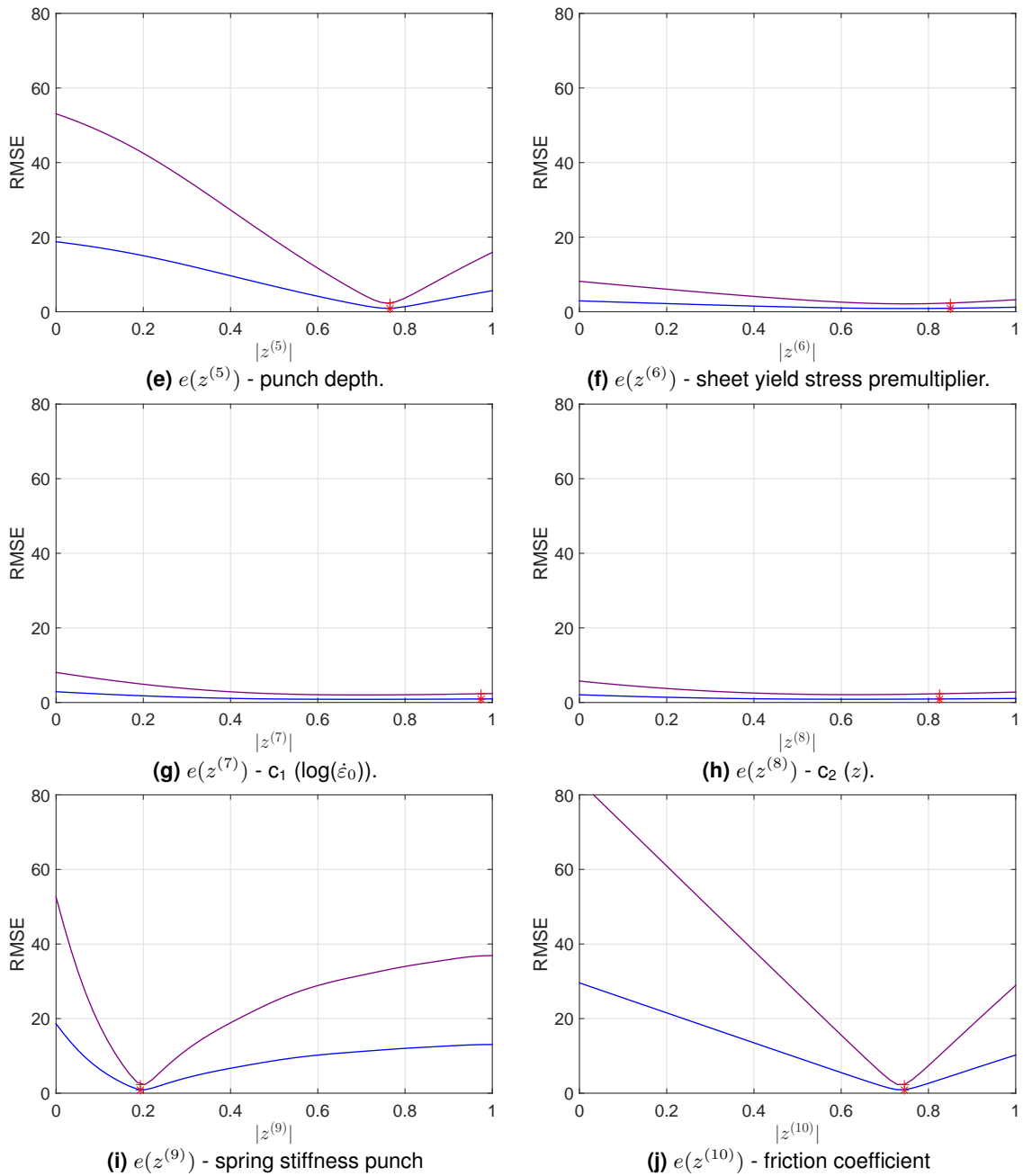


Figure 6.6: RMSE evaluated per dimension: e_t is denoted with a blue line, e_A denoted with a purple line. In red, both error function evaluated on z_p with $p = 32$ (cont.).

Evaluation of a subspace

Another point of the validation set (\mathbf{z}_p) is chosen randomly for further investigation. In Figure 6.7 the force curve from the FE-model (F_{FEM}) and the PODRBF approximation based on \mathbf{z}_p (F_{PODRBF}) are plotted. The RMSE in time ($e_t(\mathbf{z}_p)$) between the curve from the FE-model and the PODRBF approximation based on \mathbf{z}_p is 0.7473 N.

The subspace spanned by the 3 parameters which are found to be estimated accurately is examined. The subspace spanned by the punch depth, the spring stiffness of the punch and the friction coefficient ($\mathbf{Z}^{(5)} \times \mathbf{Z}^{(9)} \times \mathbf{Z}^{(10)}$) is discretized with 50 points in each dimension.

The RMSE based on time ($e_t(z^{(5)}, z^{(9)}, z^{(10)})$) is evaluated throughout this parameter subspace. The force curve based on the minimum RMSE found within this subspace (F_{inv}) is plotted using the PODRBF-model in Figure 6.7. As one can see, the force curves are very similar. When comparing F_{FEM} and F_{inv} one can see a change in slope near the maximum force, probably due to initial contact with the die. The force curve from the PODRBF-model (F_{PODRBF}) does not show this sudden change in slope.

The RMSE between the curve from the FE-model and the PODRBF approximation based on the estimated parameters is 0.5698 N. This is lower than the RMSE between the force curve from the FE-model and the PODRBF approximation based on \mathbf{z}_p .

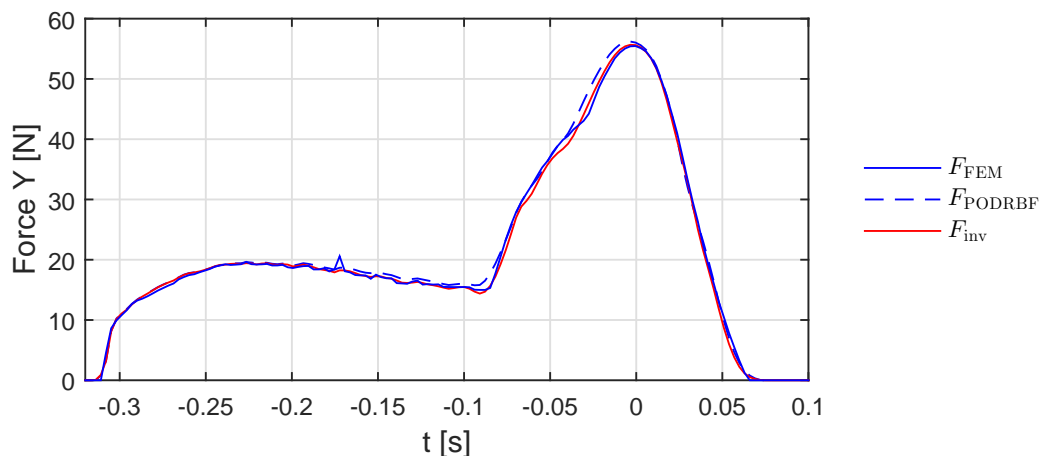


Figure 6.7: Force curves from the FE-model (F_{FEM}) and the PODRBF approximation (F_{PODRBF}) based on \mathbf{z}_p with $p = 92$ are plotted in blue. Force curve based on the estimated values for $z^{(5)}$, $z^{(9)}$ and $z^{(10)}$ with minimum RMSE in time (F_{inv}) is plotted in red.

The RMSE in time evaluated on the minimum found in each dimension is plotted in Figure 6.8. The contour plots do not show local minima. The RMSE on the minimum in $\mathbf{Z}^{(10)}$ shows the largest variation. As a result the found minimum values in that plane ($z^{(5)}$ and $z^{(9)}$) denoted with a white +-sign are the closest to the input parameters $z_p^{(5)}$ and $z_p^{(9)}$, denoted with a red *-sign.

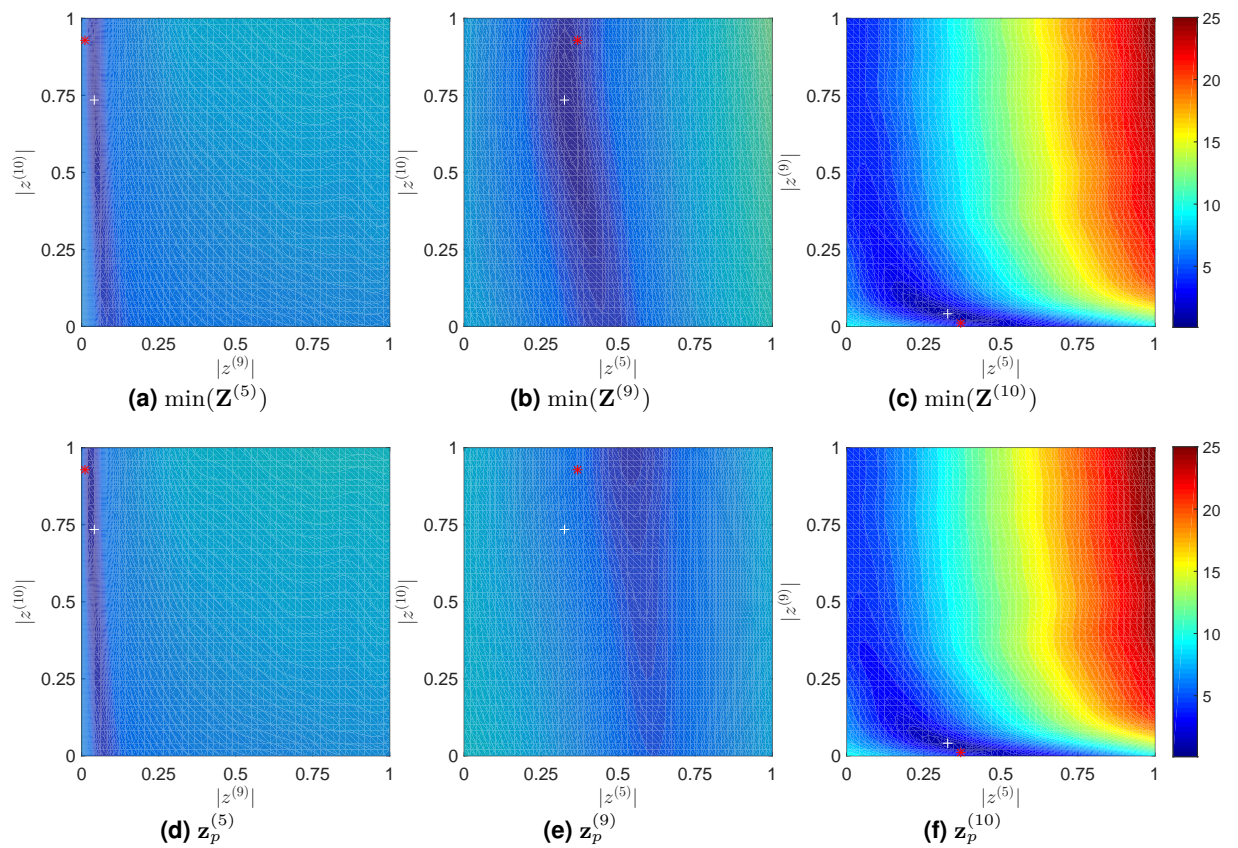


Figure 6.8: Contour plot of RMSE based on time ($e_t(z^{(5)}, z^{(9)}, z^{(10)})$). On the top: contour on found minimum in each dimension $\min(\mathbf{Z}^{(d)})$. On the bottom: contour on input parameter ($z_p^{(d)}$). The found minimum is denoted with a white + -sign, the input parameters are denoted with a red * -sign.

Inverse analysis of the test data

To do an inverse analysis on the test data the three force curve from one randomly chosen product are examined. To overcome local minima 25 different initial positions are used to see if the solution converges to the same parameter set. The parameter estimation is done with three error functions based on time and one error function based on the amplitude (e_A). The three error function based on time used are:

- the error function without any weight (e_t , equation 6.3),
- the error function with weight ($e_{t,w}$, equation 6.6),
- an extra error function with a weight of 1 on all time steps ($e_{t,w=1}$).

Using a weight of one leads the mean of the absolute difference. This is different from taking the root mean square error. This function is introduced to be able to compare the influence of the weight function objectively.

The parameter set which resulted in the lowest evaluation of the error function is chosen as the best fit. The estimated parameters based on the different error functions can be found in Table 6.9, 6.10 and 6.10. The force curves based on these estimated parameters can be found in Figure 6.9, 6.10 and 6.11 respectively. The force curve on which the parameter estimation is based is plotted for comparison. Generally the behavior of the experimental force curves is well captured by the PODRBF-model.

As expected the error function with weight function ($e_{t,w}$) generally gives the lowest error. The influence of using the weight function based on the difference between the two- and three-dimensional FE-model (equation 6.6) can be examined when comparing the last second and third columns in the table. Generally the results of introducing a weight of one ($e_{t,w=1}$) or the weight function ($e_{t,w}$) show little differences.

The sheet thickness, sheet yield stress premultiplier, c_1 and c_2 should be the same within one product. All other parameters can differ per flap. When comparing the tables with estimated parameters, especially the strain rate dependent material constants (c_1 and c_2) differ a lot.

All the values for the spring stiffness found in the force curves from the test setup are much lower than the nominal spring stiffness used. This is probably due to the compliance of the tooling.

When comparing the first and last column it can be seen that the error functions without weight, both in time and in amplitude, found the same set of input parameters. The error in amplitude is less than three times as large as the error in time, as expected from equation 6.8. This is probably due to the truncation error in the time based error function. It can thus be concluded that the truncation error has no influence on the parameter estimation. Note that on average the error function defined in the POD basis needs the fewest iterations to find a solution.

In Figure 6.11 it can be seen that large negative x -alignments can be found in the inverse analysis as well. The force curve from the test setup shows a larger negative x -alignment than can be captured by the PODRBF-model.

Table 6.1: Best fit from 25 initial positions in the parameter estimation of F_{test1} .

$z^{(d)}$	e_t	$e_{t,w=1}$	$e_{t,w}$	e_A	
clearance die/fixed die	1.28×10^{-3}	1.12×10^{-3}	1.55×10^{-3}	1.28×10^{-3}	mm
x -alignment lower part	-0.0136	-0.0136	-0.0143	-0.0136	mm
sheet thickness	0.305	0.303	0.297	0.305	mm
y -alignment die	0.000	-0.001	-0.001	0.000	mm
punch depth	1.53	1.53	1.53	1.53	mm
sheet yield stress premultiplier	0.9	1.0	1.0	0.9	-
C_1	2.99	2.57	1.62	2.99	-
C_2	0.30	0.35	0.49	0.30	-
spring stiffness punch	5246	5329	5183	5246	N/mm
friction coefficient	0.09	0.09	0.09	0.09	-
$e(\mathbf{z})$	1.519	0.985	0.753	3.240	
average iterations needed	140	188	177	101	

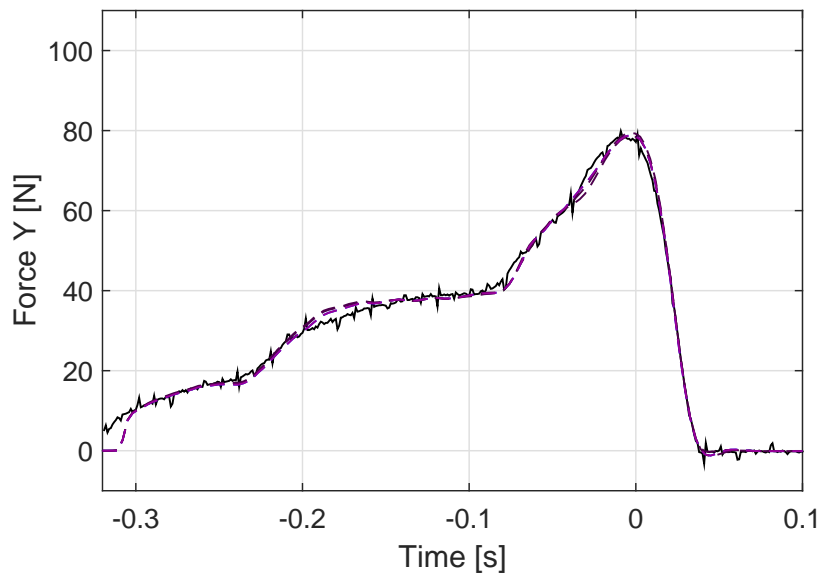
**Figure 6.9:** Force curve from the test setup ($F_{\text{test1}}(t_n)$) and the force curves from the PODRBF-model based on the estimated parameters from Table 6.1.

Table 6.2: Best fit from 25 initial positions in the parameter estimation of $F_{\text{test}2}$.

$z^{(d)}$	e_t	$e_{t,w=1}$	$e_{t,w}$	e_A	
clearance die/fixed die	3.22×10^{-3}	1.85×10^{-3}	1.11×10^{-3}	3.22×10^{-3}	mm
x -alignment lower part	-0.0132	-0.051	-0.0045	-0.0132	mm
sheet thickness	0.296	0.298	0.300	0.296	mm
y -alignment die	0.000	-0.005	-0.005	0.000	mm
punch depth	1.58	1.57	1.57	1.58	mm
sheet yield stress premultiplier	1.1	1.0	1.1	1.1	-
c_1	2.70	1.84	2.41	2.70	-
c_2	0.43	0.52	0.60	0.43	-
spring stiffness punch	7252	4603	5814	7252	N/mm
friction coefficient	0.03	0.16	0.10	0.03	-
$e(\mathbf{z})$	1.461	1.011	0.768	3.309	
average iterations needed	124	132	148	122	

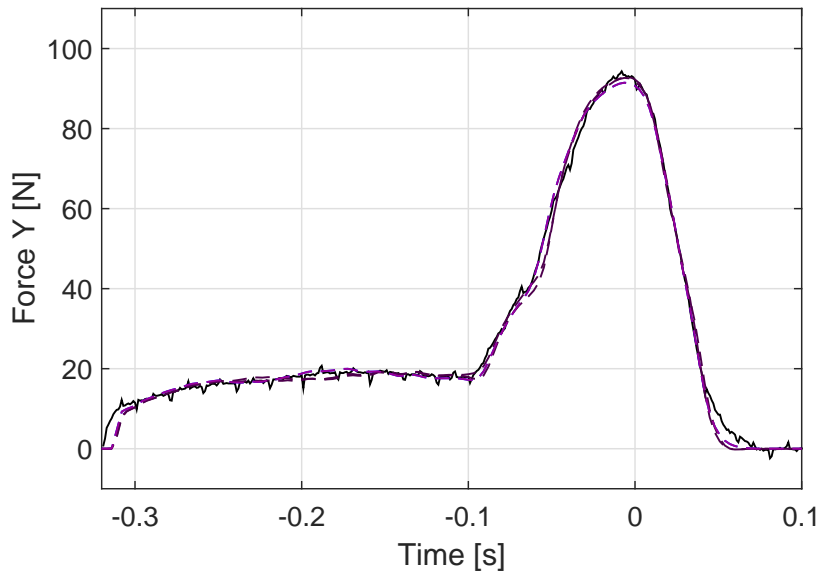
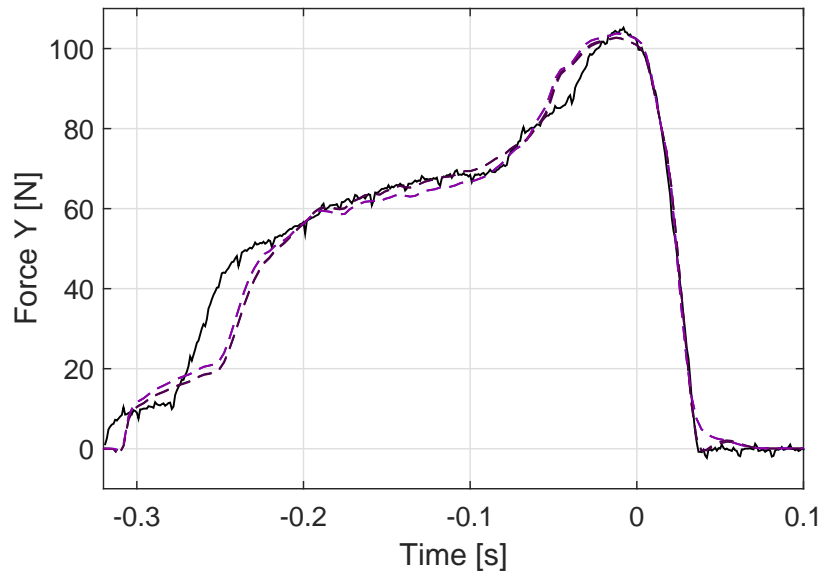
**Figure 6.10:** Force curve from the test setup ($F_{\text{test}2}(t_n)$) and the force curves from the PODRBF-model based on the estimated parameters from Table 6.2.

Table 6.3: Best fit from 25 initial positions in the parameter estimation of F_{test3} .

$z^{(d)}$	e_t	$e_{t,w=1}$	$e_{t,w}$	e_A	
clearance die/fixed die	0.05×10^{-3}	0.33×10^{-3}	0.33×10^{-3}	0.05×10^{-3}	mm
x -alignment lower part	-0.0194	-0.0192	-0.0193	-0.0194	mm
sheet thickness	0.295	0.297	0.296	0.295	mm
y -alignment die	-0.009	-0.005	-0.005	-0.009	mm
punch depth	1.53	1.52	1.52	1.53	mm
sheet yield stress premultiplier	1.1	1.1	1.1	1.1	-
C_1	1.20	1.42	1.50	1.20	-
C_2	0.38	0.57	0.51	0.38	-
spring stiffness punch	5726	5329	5327	5726	N/mm
friction coefficient	0.10	0.11	0.11	0.10	-
$e(z)$	4.304	2.309	1.955	9.082	
average iterations needed	94	107	100	76	

**Figure 6.11:** Force curve from the test setup ($F_{\text{test3}}(t_n)$) and the force curves from the PODRBF-model based on the estimated parameters from Table 6.3.

7 Conclusion

The goal of this work was to build a detailed, accurate and fast model of the bending stage, which can be used for model-based control.

With an average wall time of 0.03 s with $N_\varphi = 25$ the build PODRBF-model is fast enough to be used in an inverse analysis. Both error functions defined in time and in the POD basis are used successfully in a parameter estimation.

The PODRBF-model is detailed enough to estimate 3 parameters with 10 % accuracy. The parameters which can be estimated are:

- the punch depth,
- the spring stiffness of the punch,
- and the friction coefficient.

Large negative x -alignments of the lower part can be identified as well.

A relation between the error function in time and in the POD basis was found. The functions can be used interchangeably to estimate the process parameters. The error due to truncation has no influence on the parameter estimation. An advantage of using the error function directly in the POD basis is that the function evaluation is slightly faster. Especially for large number of iterations this can significantly decrease the computational time needed.

8 Discussion & recommendations

To improve the results of the inverse analysis a few improvements are suggested in this section.

8.1 Material model

The material constants used in the strain rate dependent material model (c_1 and c_2) should come out the same, especially when the same experimental force curve is analyzed. However as can be seen in Table 6.9, 6.10 and 6.10 the material constants show large variations. Maybe the used material model (equation 3.5) is not correct.

The material of the demonstrator product is rolled to produce the coils used in the production process. Therefore the assumption that the material is isotropic is not correct. As the flaps in the demonstrator product are not aligned but positioned in different directions, this anisotropic behavior might have an influence on the measured force curve and thus on the parameter estimation.

Only data with 12 rpm is examined in this work. However there is also test data available at a production speed of 60 rpm. The influence of using higher production speeds is not investigated in this work.

8.2 Parameter space

To obtain a more accurate PODRBF-model the parameter space should be enlarged. In Figure 6.11 it can be seen that the force curve from the test setup has a lower x -alignment than the minimum x -alignment in the parameter space.

The addition of a weight function is suggested, to take into account the difference in initial contact. However, this difference in initial contact could be captured by the PODRBF-model by increasing the maximum punch depth in combination with a small spring constant. To the maximum punch depth should therefore be increased.

The values of the initial DOE are based on a Latin hypercube sample. However, the intention was to include a fractional factorial design with two-levels and a resolution IV as well. Due to a programming mistake this fractional factorial design was not included in the parameter space. A fractional factorial design will produce points that lay on the boundaries of the parameter space.

It is therefore suggested redefine the boundaries of the parameter space and to include a fractional factorial design in the initial DOE.

8.3 POD basis

The POD basis can be improved as proposed by Chatterjee [2] by subtracting the mean of each column. For the current POD basis it was found that this gives an RMSE improvement of 0.0237 N over the total basis.

The influence of the number of time steps (N) is not studied in this work. By increasing the number of time steps, it might be possible to capture sudden changes in slope (see Figure 5.5a). However, increasing the number of time steps will imply that the number of POD-direction in the truncated basis (N_φ) will also have to be increased.

The end time set to interpolate the force curves from the FE-model ($t_N = 0.28$) should have been chosen with more care. The force curves from the FE-model do show some unexplained behavior after $t = 0.1$, therefore this end time was chosen. However, in the force curves from the test setup nothing of interest happens after $t = 0.1$.

Based on the revised initial DOE and the improvements suggested in this section a new POD-basis should be build.

8.4 Inverse analysis

As can be seen in Figure 5.6 fitting more amplitude scalars using RBF is still improving the accuracy of the PODRBF-model. It is therefore suggested to find out if the RMSE with optimized scaling

converges to a constant value, just as the PODRBF-model without optimized scaling did.

The relation between the number of POD directions in the truncated basis (N_φ) and the number of parameters that can be identified (D) is not studied. It can be of great interest if a POD direction can be related directly to certain parameter and vice versa. For example in Figure 5.2 the second POD direction (φ_2) shows behavior as seen in the force curves with negative x -alignment. A good measure for the influence of a specific parameter on a certain POD direction is the relative size of each amplitude scalar.

References

- [1] Vladimir Buljak. Proper Orthogonal Decomposition and Radial Basis Functions Algorithm for Diagnostic Procedure Based on Inverse Analysis. *FME Transactions*, 38(3):129–136, 2010.
- [2] Anindya Chatterjee. An introduction to the proper orthogonal decomposition. *Current Science*, 78(7):808–817, 2000.
- [3] Jos Havinga and a.H. van den Boogaard. Inverse Identification of Process Variations for Thin Steel Sheet Bending. *Key Engineering Materials*, 651-653:1363–1368, 2015.
- [4] Jos Havinga, A. H. van den Boogaard, and G. Klaseboer. Efficient sequential robust optimization procedure with expensive simulations. submitted to Structural and Multidisciplinary Optimization, 2015.
- [5] MSC.Software Corporation. Marc 2013.1 - Volume B: Element Library, 2013.
- [6] MSC.Software Corporation. Marc2013.1 - Volume A: Theory and User Information, 2013.
- [7] Ton van den Boogaard, Jos Havinga, and Redmer van Tijum. Model-based control of strip bending in mass production. *CIRP Annals - Manufacturing Technology*, 64(1):297–300, 2015.
- [8] J. H. Wiebenga and A. H. van den Boogaard. On the effect of numerical noise in approximate optimization of forming processes using numerical simulations. *International Journal of Material Forming*, pages 317–335, April 2013.

A Modeling in Marc Mentat

This appendix describes more elaborately how MSC Marc 2013.1 and its preprocessor Mentat are used to model the bending process. The sections A.1 and A.2 describe the differences between the two-dimensional and three-dimensional model respectively. Section A.3 describes how the contact between different bodies is modeled. Lastly the numerical settings used in the analysis are given in section A.4.

A.1 2D model

In the two-dimensional model a plane strain situation is assumed. For the sheet element type 11 is used (Figure A.2a). These are rectangular plane strain elements which are fully integrated (Q4). This means each element consists four nodes and the stiffness matrix is found using four-point Gaussian integration. It is known that shear locking can occur when using these elements. To overcome problems the mesh is refined around the bending area as can be seen in Figure A.1. The number of elements used is 200 in x -direction (udiv) and 15 in y -direction (vdiv), so 3000 in total.

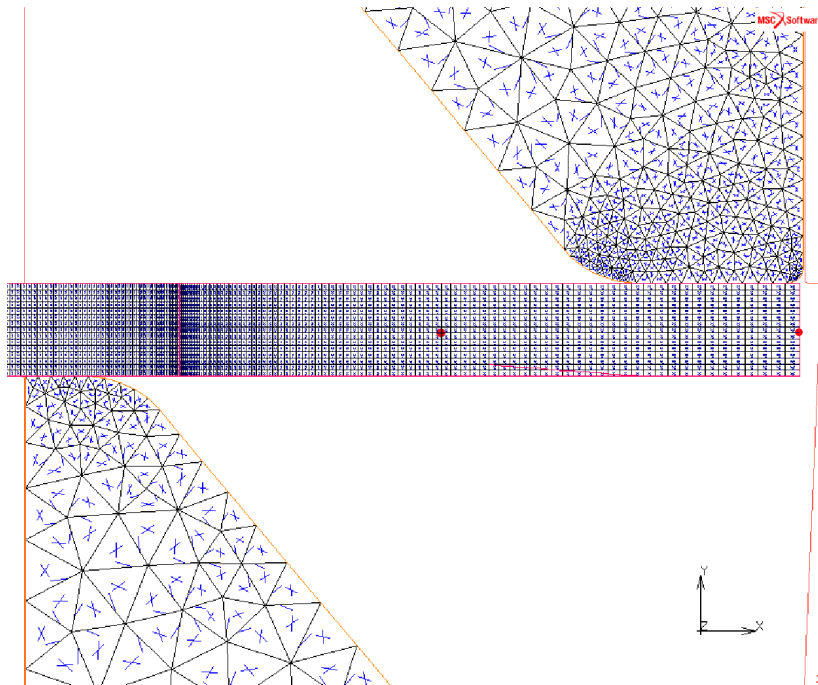


Figure A.1: Snapshot of the FE-model. The red dots denote the nodes on which the angle calculation is based.

For the punch and die element type 6 is used (Figure A.2b). These are triangular plane strain fully integrated elements (CST). Each element consists of 3 nodes. To obtain the stiffness matrix a one point integration at the centroid is used. To obtain the mass matrix a four-point Gaussian integration is done. Within the elements bi-linear interpolation functions are used which results in a constant strain throughout element. This results in poor shear behavior and locking near incompressible behavior.

All other contact bodies are modeled as rigid.

A.2 3D model

In the three-dimensional model all contact bodies except for the sheet are modeled as rigid. To model the elasticity of the die and the punch the rigid bodies are connected to a spring.

For the sheet element type 7 is used. These are rectangular solid, sometimes called brick, elements. The elements are fully integrated using an eight-point Gaussian integration and consist of 8 nodes. Tri-linear interpolation is used within the element. As for the two-dimensional elements, also in three-dimensions shear locking behavior can occur. The sheet is meshed with 150 elements in x -direction (udiv), 12 elements y -direction (vdiv) and 10 elements in z -directions. This give a total

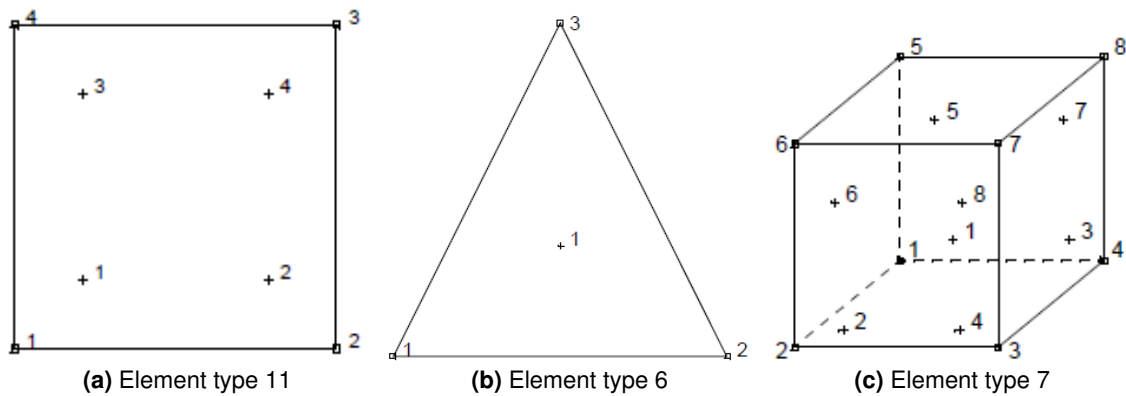


Figure A.2: Schematic representation of used elements with nodes (□) and integration points (+). [5]

of 18000 elements. Again the mesh in x -direction is concentrated around the bending area. The three-dimensional model has large computational costs, the wall time is roughly 20 times as large for 3D when compared to 2D. Therefore it is chosen to use the least elements as possible. The number of elements in x -direction is chosen as such that there is minimum penetration of the punch in the sheet during free bending.

To obtain the weight function in section 6.1 the same number of elements is used in the sheet in the two-dimensional and three-dimensional model (see Figure 6.1).

A.3 Contact modeling

To model the contact MarcMentat gives the choice between node-to-segment and segment-to-segment contact [6]. When using segment-to-segment contact sticking of the sheet to the punch occurred frequently due to a stress-based separation criterion. This was not possible to overcome by using different numerical settings. Therefore the choice was made to use node-to-segment contact. The optimization of the contact equations was set off, so that generally the region with lower node numbering comes into contact with the region with higher node numbering. The sheet is meshed first and has therefore the lowest node numbering. As the sheet has the finest mesh penetration of any contact body with higher numbering is most likely to be detected. The contact detection distance tolerance was left to the default of $1/20$ of smallest edge of the surrounding rectangle set up in the global coordinate system, resulting in 2.61450×10^{-4} . To leave the geometry unchanged the choice is made to use no stress free projection upon initial contact.

Once the two bodies are in contact they can either stick or slip. To determine if either sticking or slipping occurs a shear bi-linear model is used. The slip threshold is the displacement below which sticking is simulated. This is left to the default of 0.0025 times the average edge length of the finite elements defining the deformable contact bodies, resulting in 1.57481×10^{-4} . The choice is made to use finite sliding. The separation of two nodes is based on nodal forces. The force to cause separation is set to 1×10^{-4} .

A.4 Analysis

In the FE-analysis adaptive time stepping is used instead of using a fixed time stepping. When using an adaptive time step this allows for cutbacks when the convergence tolerance is not met. The minimum number of recycles is set to 0 and the maximum to 10. A full Newton-Raphson iterative procedure is used to find a solution.

The Updated Lagrange approach for large strain is used. Marc automatically uses Cauchy (true) stress and logarithmic strain with the Updated Lagrange formulation.

Spring back is an important behavior to model the final angle correctly. Therefore the plastic procedure is chosen to be multiplicative, which means the deformation gradient is split into an elastic and a plastic part.

The convergence of the solution is tested based on the relative residuals or displacements. This choice is made because relative residual force tolerance testing does not work in a stress-free motion. And relative displacement tolerance testing does not work in case of springback.

The relative force tolerance is set to 0.01. Thus,

$$\frac{\|F_{\text{residual}}\|_{\infty}}{\|F_{\text{reaction}}\|_{\infty}} < 0.01 \quad (\text{A.1})$$

where $\|F\|_{\infty}$ indicates the component of F with the highest absolute value. In the node-to-segment contact algorithm the node in contact is skipped in the procedure of calculating the procedure. The contact force is however considered as candidate for the maximum reaction force [6].

The relative displacement tolerance is set to 0.01. Thus,

$$\frac{\|\delta u\|_{\infty}}{\|\Delta u\|_{\infty}} < 0.01 \quad (\text{A.2})$$

where Δu is the displacement increment vector and δu is the correction to the incremental displacement vector. Disadvantage of this approach is that it results in at least one iteration [6].

B Parameter study (continued)

B.1 All parameters and their values

In the table below an overview of all parameters with their minimum, maximum and nominal values can be found.

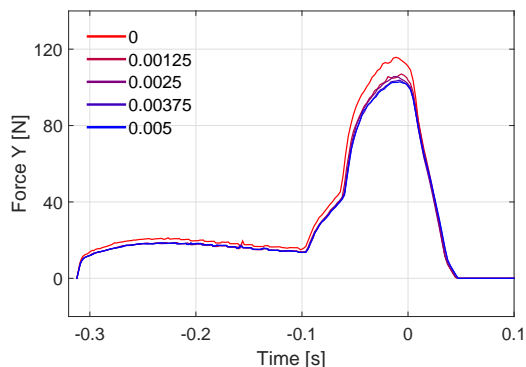
Table B.1: Variables in FE-model and corresponding minimum, maximum and nominal values.

Variable	Description	min	nominal	max	unit
Alignment					
VAR01	left clearance punch/blankholder	0	0.0025	0.005	mm
VAR02	right clearance punch/blankholder	-	=VAR01	-	mm
VAR03	left clearance die/fixed die	0	0.002	0.004	mm
VAR04	right clearance die/fixed die	-	=VAR03	-	mm
VAR05	x -alignment lower part (die & fixed die)	-0.0195	0.0005	0.0205	mm
VAR06	x -alignment cutting (sheet length)	-0.2	0	0.01	mm
VAR10	sheet thickness (y -alignment upper part)	0.29	0.3	0.31	mm
VAR11	y -alignment die	-0.02	0	0	mm
VAR12	punch depth (δ_{punch})	1.5	1.56	1.6	mm
VAR13	$K \cdot R$ (Crank, punch movement)	-	18.980075	-	-
VAR14	$\Delta\alpha$ (Crank, punch movement)	-	dependent	-	-
VAR15	λ (Crank, punch movement)	-	0.085	-	-
VAR16	T (period, 60/rpm)	1	5	5	1/s
VAR18	blank holder force	-50	-300	-500	N
VAR19	sheet width	1.4	1.5	1.6	mm
Material					
VAR20	sheet Poisson ratio	0.29	0.3	0.31	-
VAR21	sheet Young's modulus	190	210	230	GPa
VAR22	sheet yield stress premultiplier	0.9	1	1.1	-
VAR23	c_1 strain rate dependent model	1	1.63	5	-
VAR24	c_2 strain rate dependent model	0.1	0.437667	1	-
VAR25	tooling Poisson ratio	0.29	0.3	0.31	-
VAR26	tooling Young's modulus	200	210	220	GPa
VAR27	spring stiffness punch (γ_1)	1000	25898	35000	N/mm
VAR28	spring stiffness die (γ_2)	40000	54078	60000	N/mm
VAR29	friction coefficient punch/blankholder, die/fixeddie	0	0.13	0.2	-
VAR30	friction coefficient tooling/sheet	0	0.12	0.2	-
VAR31	friction coefficient punch/fixeddie	0	0.13	0.2	-
Geometric					
VAR40	fillet radii tooling	-	0.01	-	mm
VAR41	right radius fixed die	10	20	50	mm
VAR42	fillet radius punch	-	0.05	-	mm
Numerical					
VAR50	element class sheet	-	4	-	-
VAR51	element type sheet	-	11	-	-
VAR52	udiv cup (x -direction)	-	40	-	-
VAR53	udiv sheet (x -direction)	-	2x80	-	-
VAR54	vidv sheet (y -direction)	-	15	-	-

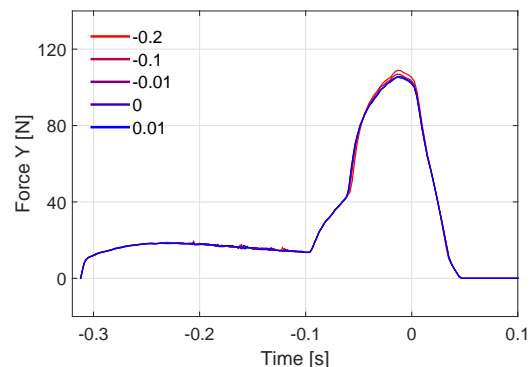
B.2 Force curves for less influential parameters

The force curves based on varying the remaining parameters are presented in this section. Hence, below one can find Figure 4.3 continued.

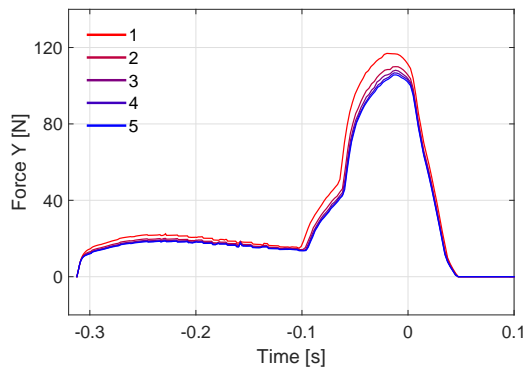
Some parameters seem to have a large influence in outcome of the force curve as well. The clearance between the punch and the blank holder only has a large influence when it is 0. As this is not a realistic case the parameter is left out of the parameter space. The period (T) has a large influence but is not incorporated in the parameter space due to the time dependency of the POD basis. The different sheet widths have linear influence on the outcome of the force curve. This can be incorporated by premultiplying the entire force curve. Therefore there is no need in including this parameter in the parameter space. As described in section 4.2 all the friction coefficients are set to the same value in the parameter space. Hence, the friction coefficients between the tooling and the sheet and between the punch and the fixed die are incorporated in the parameter space.



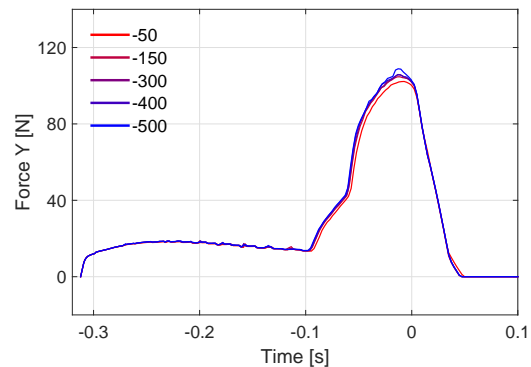
(a) VAR01 - clearance punch/blankholder.



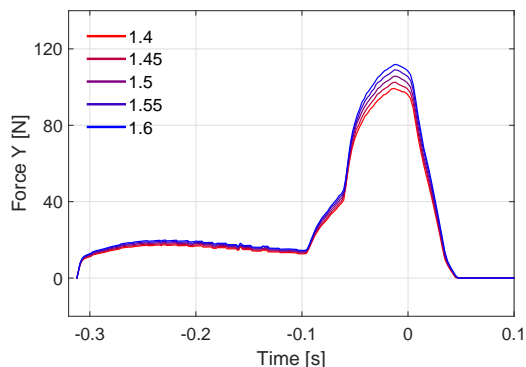
(b) VAR06 - x -alignment cutting (sheet length).



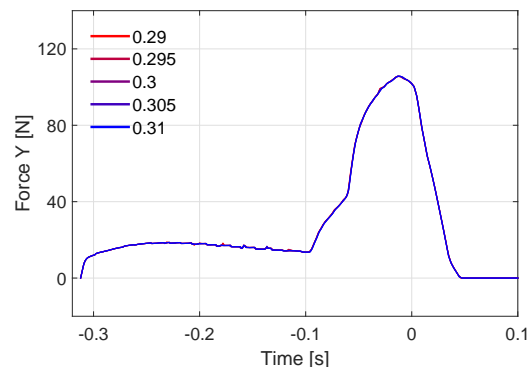
(c) VAR16 - period, scaled to $T = 5$ s.



(d) VAR18 - blankholder force.

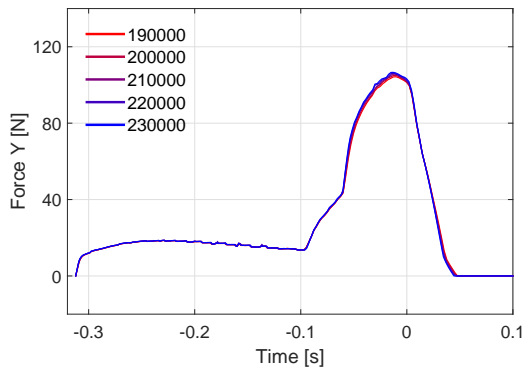


(e) VAR19 - sheet width.

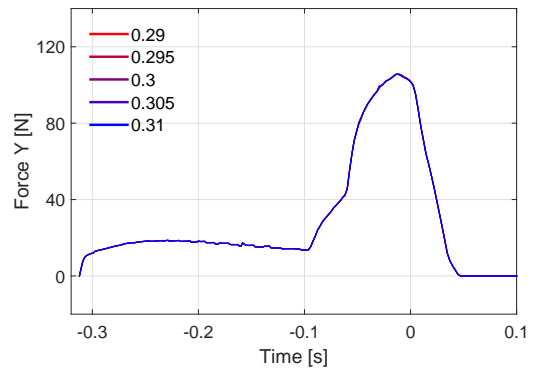


(f) VAR20 - sheet Poisson ratio.

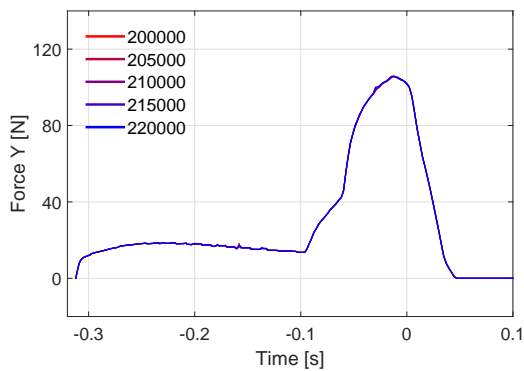
Figure B.1: FEM curves for less influential parameters.



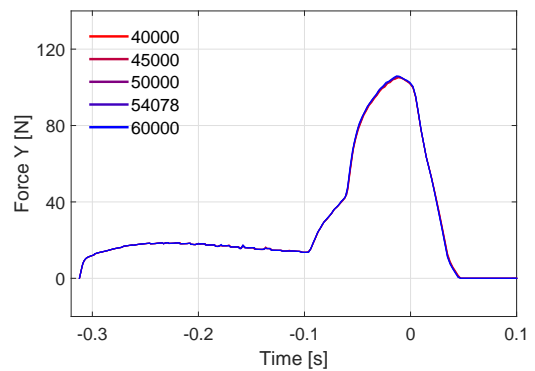
(g) VAR21 - sheet Young's modulus.



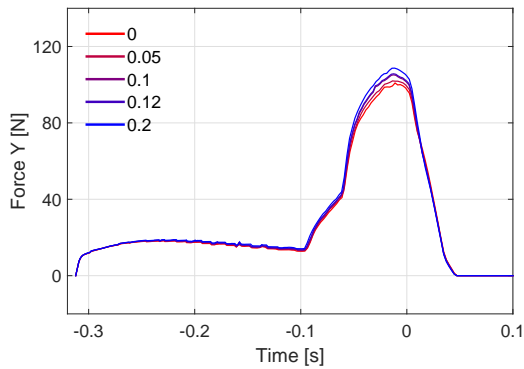
(h) VAR25 - tooling Poisson ratio.



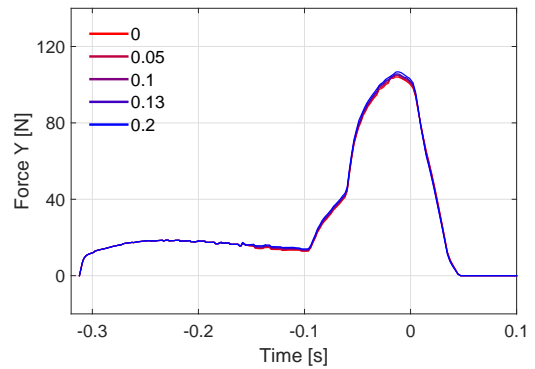
(i) VAR26 - tooling Young's modulus.



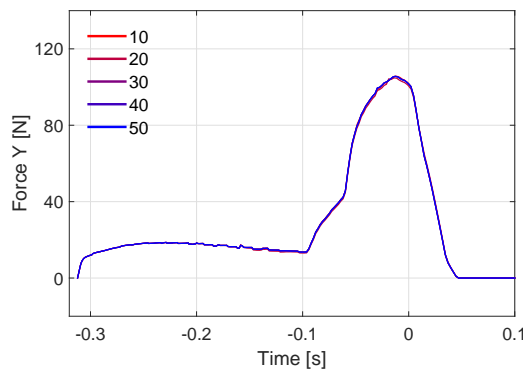
(j) VAR28 - spring stiffness die.



(k) VAR30 - friction coefficient tooling/sheet.



(l) VAR31 - friction coefficient punch/fixe die.



(m) VAR41 - right radius fixed die.

Figure B.1: FEM curves for less influential parameters (cont.).

C Parameter estimation

Table C.1 summarizes the results of the parameter estimations based on the validation set. The results are based on estimating the input parameters:

- For each point (z_p) in the validation set: $p = 1..100$,
- The error function is based on time (e_t) and on amplitude (e_A) without a weight function,
- The starting position is varied: $[0 \ 0.5 \ 1]$,
- The number of parameters to be identified is varied: $D = 1..10$,
- Which parameter(s) to be identified d is chosen randomly.

From each starting position the best fit is chosen as the estimated parameter $z^{(d)}$ which resulted in the lowest RMSE. The difference between each best fit and the input parameter $z_p^{(d)}$ is averaged and presented in Table C.1. All parameters are normalized, therefore the values can be interpreted as percentages. Note that the estimation with $D = 1$ is averaged over 10 estimations, whereas the estimation with $D = 10$ is averaged over 100 estimations.

When using an error function in time to estimate one parameter, the average number of iterations needed was 12.8 with 49.6 function evaluations. When 10 parameters were estimated an average of 147.8 iterations with 1794 function evaluations were needed.

When using an error function based on the amplitude to estimate one parameter, the average number of iterations needed was 13 with 51 function evaluations. When 10 parameters were estimated an average of 143 iterations with 1741 function evaluations were needed.

Table C.1: Average error in parameter estimation based on z_p .

$z^{(d)} =$	D = 1		D = 2		D = 3		D = 4		D = 5	
	<i>t</i>	<i>A</i>								
clearance	0.10	0.20	0.24	0.19	0.18	0.29	0.24	0.33	0.25	0.28
die/fixed die										
x-alignment	0.31	0.17	0.06	0.14	0.09	0.12	0.16	0.21	0.19	0.12
lower part										
sheet thickness	0.11	0.10	0.16	0.13	0.13	0.22	0.23	0.17	0.17	0.16
y-alignment die	0.04	0.08	0.10	0.10	0.11	0.16	0.22	0.19	0.25	0.22
punch depth	0.03	0.03	0.03	0.06	0.05	0.02	0.06	0.06	0.08	0.06
sheet yield	0.07	0.07	0.08	0.10	0.08	0.07	0.09	0.11	0.09	0.11
stress pre-multiplier										
c1	0.08	0.11	0.09	0.06	0.09	0.13	0.15	0.16	0.17	0.15
c2	0.04	0.08	0.14	0.10	0.16	0.15	0.17	0.14	0.19	0.20
spring stiffness	0.08	0.05	0.03	0.05	0.03	0.03	0.06	0.08	0.08	0.05
punch										
friction coefficient	0.05	0.04	0.06	0.06	0.06	0.07	0.07	0.05	0.05	0.04
<i>average</i>	0.09	0.09	0.10	0.10	0.10	0.13	0.14	0.15	0.15	0.14

Table C.1: Average error in parameter estimation based on z_p (cont.).

$z^{(d)} =$	D = 6		D = 7		D = 8		D = 9		D = 10		<i>average</i>	
	<i>t</i>	<i>A</i>	<i>t</i>	<i>A</i>								
clearance	0.27	0.25	0.29	0.30	0.33	0.31	0.31	0.33	0.34	0.34	0.25	0.28
die/fixed die												
x-alignment	0.18	0.20	0.19	0.19	0.19	0.19	0.20	0.16	0.16	0.14	0.17	0.16
lower part												
sheet thickness	0.23	0.24	0.25	0.24	0.26	0.27	0.26	0.30	0.29	0.27	0.21	0.21
y-alignment die	0.24	0.22	0.27	0.23	0.23	0.25	0.26	0.28	0.25	0.28	0.20	0.20
punch depth	0.08	0.06	0.11	0.07	0.09	0.10	0.09	0.09	0.09	0.08	0.07	0.06
sheet yield	0.14	0.11	0.12	0.16	0.13	0.15	0.16	0.16	0.17	0.16	0.11	0.12
stress pre-multiplier												
c1	0.20	0.23	0.21	0.21	0.24	0.21	0.25	0.21	0.25	0.23	0.17	0.17
c2	0.21	0.21	0.26	0.24	0.28	0.27	0.32	0.27	0.30	0.29	0.21	0.20
spring stiffness	0.08	0.08	0.06	0.08	0.06	0.09	0.06	0.06	0.05	0.06	0.06	0.06
punch												
friction coefficient	0.06	0.05	0.09	0.07	0.07	0.06	0.08	0.06	0.07	0.07	0.07	0.06
<i>average</i>	0.17	0.16	0.19	0.18	0.19	0.19	0.20	0.19	0.20	0.19		